HHS Public Access

Author manuscript

Nat Commun. Author manuscript; available in PMC 2015 July 27.

Published in final edited form as:

Nat Commun. ; 6: 6118. doi:10.1038/ncomms7118.

Coexistent ARID1A-PIK3CA mutations promote ovarian clear-cell tumorigenesis through pro-tumorigenic inflammatory cytokine signaling

Ronald L. Chandler[1,3,*], **Jeffrey S. Damrauer**[1,3,*], **Jesse R. Raab**[1,3], **Jonathan C. Schisler**[4,5], **Matthew D. Wilkerson**[1,3], **John P. Didion**[1,3], **Joshua Starmer**[1,3], **Daniel Serber**[1,3], **Della Yee**[1,3], **Jessie Xiong**[3], **David B. Darr**[3], **Fernando Pardo-Manuel de Villena**[1,3], **William Y. Kim**[1,2,3], and **Terry Magnuson**[1,3,+]

[1]Department of Genetics, University of North Carolina at Chapel Hill, Chapel Hill, NC 27599

[2]Department of Medicine, University of North Carolina at Chapel Hill, Chapel Hill, NC 27599

[3]Lineberger Comprehensive Cancer Center, University of North Carolina at Chapel Hill, Chapel Hill, NC 27599

[4]McAllister Heart Institute, University of North Carolina at Chapel Hill, Chapel Hill, NC 27599

[5]Department of Pharmacology, University of North Carolina at Chapel Hill, Chapel Hill, NC 27599

Abstract

Ovarian clear-cell carcinoma (OCCC) is an aggressive form of ovarian cancer with high *ARID1A* mutation rates. Here we present a mutant mouse model of OCCC. We find that *ARID1A* inactivation is not sufficient for tumor formation, but requires concurrent activation of the phosphoinositide 3-kinase catalytic subunit, PIK3CA. Remarkably, the mice develop highly penetrant tumors with OCCC-like histopathology, culminating in hemorrhagic ascites and a median survival period of 7.5 weeks. Therapeutic treatment with the pan-PI3K inhibitor, BKM120, prolongs mouse survival by inhibiting tumor cell growth. Cross-species gene expression comparisons support a role for IL-6 inflammatory cytokine signaling in OCCC pathogenesis. We further show that *ARID1A* and *PIK3CA* mutations cooperate to promote tumor growth through sustained IL-6 overproduction. Our findings establish an epistatic relationship between SWI/SNF chromatin remodeling and PI3K pathway mutations in OCCC and demonstrate that these

+Address inquiries to trm4@med.unc.edu.
*denotes co-first authorship

Author Contribution Statement:
R.L.C conceived this study, developed the hypothesis, and wrote the manuscript with supervision and gracious support from T.M. R.L.C., J.S.D., J.C.S, D.B.D., F.P.M.V., W.Y.K., and T.M. contributed to the experimental design. R.L.C., J.S.D., J.C.S., D.S., D.Y., J.X. performed the experiments. J.R.R. and J.P.D. performed the computational analysis with conceptual advice from M.D.W and J.S. All of the authors commented on the manuscript.

Competing Financial Interests Statement:
The authors declare no competing financial interests.

Accession codes:
Microarray gene expression datasets generated in this study were deposited in the Gene Expression Omnibus (GEO) repository under the accession code: GSE57380.

pathways converge on pro-tumorigenic cytokine signaling. We propose that ARID1A protects against inflammation-driven tumorigenesis.

Keywords

ARID1A; PIK3CA; IL-6; Ovarian Cancer; PI3K pathway; SWI/SNF

Introduction

Epithelial ovarian cancer (EOC) ranks as the 5th leading cause of cancer death among women[1]. EOC consists of four major histologic tumor subtypes (serous, clear-cell, endometrioid, or mucinous) and originates from the coelomic epithelium, which is the precursor to the ovarian surface epithelium (OSE) and Müllerian ductal epithelium[2]. The salpinge or fallopian tube of the Müllerian epithelial anlage is the more definitive source of serous EOC[3]. Endometriotic explants originating from more distal sites in the Müllerian epithelial anlage may have some propensity to give rise to clear cell or endometrioid EOC in humans, but this alternate mechanism of pathogenesis has not been thoroughly investigated[4, 5].

In addition to histologic feature, each EOC subtype can be further classified into two distinct groups on the basis of disease progression, metastatic potential, and molecular signature, with low-grade serous, clear-cell, mucinous and endometrioid subtypes being classified as Type I tumors and the high-grade serous subtype as Type II tumors[6]. In general, Type I tumors account for up to 25% of EOCs, are genomically stable and have lower metastatic potential than Type II tumors, which constitute most of the remaining EOC cases[6]. In addition, *KRAS*, *BRAF*, *PIK3CA*, *PTEN*, and *CTNNB1* (β-CATENIN) mutations have historically been associated with Type I tumors at varying frequencies, whereas Type II tumors are largely defined by high frequency *TRP53* (p53) mutations and chromosome instability[6, 7, 8]. Therefore, EOC consists of a heterogeneous group of cancers, each with unique clinical challenges and biology.

Ovarian clear-cell carcinoma (OCCC) is the most common Type I tumor, accounting for 5–25% of all EOC cases, with incidence varying between populations[9, 10, 11]. Endometriosis is recognized as a significant risk factor for OCCC[12, 13, 14]. Among all EOC subtypes, OCCC has the worst prognosis if diagnosed at an advanced stage of disease because of poor response rates to platinum-based chemotherapy[9, 10, 15, 16]. Consequently, survival rates for women with advanced stage OCCC are low[9, 10, 15, 16]. Although OCCC is the second leading cause of death from ovarian cancer, the etiology and pathogenesis of this devastating disease are poorly understood.

Recent genome sequencing efforts support a strong genetic contribution to OCCC etiology based upon the discovery of high frequency (up to 50%) *ARID1A* tumor mutations[17, 18]. *ARID1A* is also somatically mutated in another Type I EOC, endometrioid carcinoma, and several other gynecologic cancers, including uterine clear-cell and endometrioid carcinomas, cervical carcinoma, and uterine carcinosarcoma[19, 20]. Additional tumor sequencing studies have detected recurrent *ARID1A* mutations in several non-gynecologic cancers and, taken

together, components of the SWI/SNF complex are mutated in at least 20% of human cancer[19, 21, 22, 23]. ARID1A is a subunit within the SWI/SNF chromatin remodeling complex that facilitates target substrate recognition, however, its role in OCCC tumor initiation and progression has yet to be fully elucidated[24].

Genetically engineered mouse models offer the opportunity to investigate the contribution of genetic factors to EOC etiology and pathogenesis[25]. In this regard, early research using mouse models of EOC established causative roles for coexistent mutations in PTEN and KRAS or PTEN and WNT/β-CATENIN pathways in endometrioid EOC[7, 8]. Recently, Guan *et al*. reported a mouse model of endometrioid EOC involving coexistent mutations in *PTEN* and *ARID1A*[26]. In this study, we describe a new mouse model that genetically and histologically resembles human OCCC and functionally implicates coexistent *ARID1A* and *PIK3CA* mutations in cancer causation. We further provide new mechanistic insight into OCCC pathogenesis by establishing a functional link between coexistent *ARID1A-PIK3CA* mutations and IL-6 signaling.

Results

Generation of a novel *Arid1a* conditional allele

To establish a functional role for *ARID1A* mutations in ovarian clear-cell tumorigenesis, we generated a novel *Arid1a* conditional allele (*Arid1a*^{fl}) by inserting loxP sites flanking exons 5 and 6 in *ARID1A* (Fig. 1A,B). *Arid1a-null* embryos die around gastrulation, thus they are not amenable to efficient protein extraction[27]. In light of its early embryonic lethality, we monoalleliclly inactivated *ARID1A* in embryonic tissues (via *Sox2Cre*[28]) to verify our *Arid1a*^{fl} allele in the whole animal. Using this approach, we observed an expected 50% reduction in total protein from whole embryo lysates (Fig. 1C,D). We next sought to inactivate ARID1A in the OSE. To do this, we employed the intrabursal Adenovirus CRE-mediated (AdCRE) recombination system[7, 29]. Efficient CRE-mediated genetic recombination was consistently observed in the OSE and outer epithelial layers of tissues confined to the bursal space (Fig. 1F,H,I). We performed a series of intrabursal AdCRE injections on two independent cohorts of *Arid1a*$^{fl/fl}$ mice (n=42) and followed them for approximately one year. The mice remained tumor-free with no significant changes in survival, other than age-related mortality, similar to the phenotypes reported by Guan *et al*.[26] (Supplementary Fig. 1). The observation that ARID1A loss does not lead to tumor formation supports the notion that *ARID1A* mutations require additional mutational “hits” in the OSE before tumorigenesis can ensue[26].

Coexistent *ARID1A-PIK3CA* mutations initiate ovarian cancer

To explore this further, we focused on the cancer proto-oncogene, PIK3CA (Phosphatidylinositol-4,5-bisphosphate 3-kinase, catalytic subunit alpha or p110α), which also has high OCCC mutation rates[30, 31]. Recently, coexistent *ARID1A-PIK3CA* mutations were reported in gastric cancer[32]. Additionally, it has been observed that OCCC tumors harboring *PIK3CA* mutations display concomitant loss of ARID1A immunoreactivity, raising the possibility that *ARID1A* and *PIK3CA* mutations frequently co-occur in OCCC[33]. To understand the degree of mutational co-occurrence, we compared the incidence of

ARID1A and/or *PIK3CA* mutations in available tumor datasets curated in The Cancer Genome Atlas (TCGA) to OCCC tumor sequencing data[17]. We found that the majority of cancers carry genetic alterations in one of these genes, however the rate of *ARID1A-PIK3CA* mutational co-occurrence (33%; pval<0.05) is highest in OCCC (Fig. 2A).

PIK3CA tumor mutations often result in an H1047R 'hotspot' substitution within the kinase domain, generating a catalytically active protein[34]. *PIK3CA* amplification also frequently occurs in EOC[30]. To investigate the effect of PIK3CA alterations on ovarian tumorigenesis, we used the CRE-inducible *(Gt)Rosa26Pik3ca*^{*H1047R} allele[35] to drive PIK3CA^{H1047R} expression from the *Rosa26* locus. We observed multifocal sites of epithelial hyperplasia in the OSE of AdCRE injected *(Gt)Rosa26Pik3ca*^{*H1047R} mice, but no tumor formation (Table 1). Intrabursal AdCRE induction of PIK3CA^{H1047R}, under the control of the endogenous promoter, also led to OSE hyperplasia in the mouse[36], suggesting that constitutive overexpression of PIK3CA^{H1047R} from the *Rosa26* locus does not further augment this process.

We next evaluated the combinatorial effects of ARID1A loss and PIK3CA activation by performing AdCRE injections into the ovarian bursa of *Arid1a*$^{fl/fl}$*;(Gt)Rosa26Pik3ca*^{*H1047R} mice. In stark contrast to the single mutants, *Arid1a*$^{fl/fl}$*;(Gt)Rosa26Pik3ca*^{*H1047R} mice rapidly developed primary ovarian tumors and showed evidence of abdominal distension, warranting sacrifice with a median latency period of 7.5 weeks post-AdCRE injection (Fig. 2J–M). Evidence for tumor-specific ARID1A loss and PIK3CA^{H1047R} expression or PI3K pathway activation was detected by PCR amplification of tumor cDNA or by tumor immunohistochemistry (IHC) for ARID1A and phosphorylation of AKT at serine 473 (P-AKT S473) (Fig. 2B–I). Increased morbidity coincided with the presentation of hemorrhagic ascites (Fig. 2J,L). Peritoneal metastases were detected in approximately 50% of the double mutants, often residing near the contralateral, uninjected ovary (Fig. 2K, see Table 1). Distant metastases beyond the abdominal cavity were not evident upon gross examination. We did not find evidence for genome instability in *Arid1a*$^{fl/fl}$*;(Gt)Rosa26Pik3ca*^{*H1047R} tumor samples using mouse high-density SNP arrays (Supplementary Fig. 2).

ARID1A haploinsufficiency does not lead to tumor formation

Several studies point to a gene dose-dependent role for ARID1A in tumor suppression given the high incidence of heterozygous tumor mutations in cancer[19]. To determine if an ARID1A haploinsufficiency coupled with PI3K pathway activation leads to ovarian cancer in our model, we performed AdCRE injections on *Arid1a*$^{fl/+}$*;(Gt)Rosa26Pik3ca*^{*H1047R} mice. OSE hyperplasia was observed in 5 of 7 *Arid1a*$^{fl/+}$*;(Gt)Rosa26Pik3ca*^{*H1047R} mice, but evidence of tumor formation was not detected after the 11-week observation period, similar to the *(Gt)Rosa26Pik3ca*^{*H1047R} only cohort (Fig. 2N,O, see Table 1). These data are consistent with the observation that most OCCC tumors carrying heterozygous mutations in *ARID1A* show loss of ARID1A immunoreactivity and support the notion that additional mechanisms lead to loss of ARID1A protein expression in OCCC[18, 37]. Thus, ARID1A likely follows the classical "two-hit" model of tumor suppression in OCCC.

Therapeutic PIK3CA inhibition prolongs animal survival

We next sought to examine the role of continued PIK3CA activation in the progression of ARID1A-deficient ovarian tumors and determine whether therapeutic PIK3CA inhibition would inhibit tumor cell growth and improve animal survival. Primary EOC tumor cells were isolated from the exfoliated tumor cell aggregates present in ascites fluid of tumor-burdened *Arid1a$^{fl/fl}$;(Gt)Rosa26Pik3ca^{*H1047R}* mice and subcultured using established methods (Fig. 3A). Isolated tumor cells displayed ARID1A loss and heightened PI3K signaling, as evidence by loss of ARID1A immunoreactivity and increased P-AKT S473 levels compared to normal OSE cells (Fig. 3B). Administration of the pan-class I PI3K inhibitor, BKM120 (*Buparlisib*) led to a dose-dependent decrease in P-AKT S473 and concomitant reduction in tumor cell viability (IC_{50}= 0.96 +/− 0.25 μM) (Fig. 3C,D). We next administered chow-fed BKM120 to *Arid1a$^{fl/fl}$;(Gt)Rosa26Pik3ca^{*H1047R}* mice for 3 weeks, starting at week 4 post-AdCRE injection. The effectiveness of BKM120-dependent inhibition of PI3K signaling in chow-fed mice was accessed by tumor IHC for phosphorylation of the S6 Ribosomal Protein at serine 235/236 (P-S6) (Fig. 3E). BKM120 treatment led to reduced P-S6 levels and extended the median latency period by 3.5 weeks (Fig. 3E,F). These data indicate that therapeutic PI3K inhibition promotes animal survival by inhibiting tumor cell growth, thus providing strong rationale for the use of PI3K inhibitors in OCCC treatment.

Mouse ovarian tumors manifest OCCC-like histopathology

Cardinal histopathological features of human OCCC include cells with clear cytoplasm, stromal hyalinization, solid, papillary, or tubulocystic tumor architectural patterns, and HNF1β immunoreactivity[38]. The ovarian tumors observed in *Arid1a$^{fl/fl}$;(Gt)Rosa26Pik3ca^{*H1047R}* mice were predominately solid in appearance with some papillary areas (Fig. 4A–D, see Table 1). Tubulocystic patterns were rarely observed (Fig. 4E, see Table 1). Neoplastic cells with clear cytoplasm, prominent nucleoli, and pleomorphic nuclei were observed in the tumors (see high magnification in Fig. 4A'-C'). Elongated spindle-shaped cells with finely vacuolated cytoplasm were observed embedded in hyalinized matrix. Solid clear-cell carcinomas were observed directly attached to the ovarian surface (Fig. 4A). We rarely observed tumor cells organized into bands of glandular epithelium with distinct borders, and, in general, the tumors appeared poorly differentiated and highly disorganized. Primary tumor masses ranged from approximately 100 mg to over 1 g (Fig. 4J). Differences in tumor size, metastatic potential, or morbidity did not correlate with any particular histologic feature.

In human OCCC, neoplastic cells that line luminal spaces often assume a 'hobnail' appearance, which crudely resembles a nucleus standing on the tip of a cytoplasmic stalk. Hobnail cells were often observed on the tumor periphery in regions where tumor cell exfoliation into luminal regions was occurring (Fig. 4D, I, K). Exfoliated, metastatic tumor cell aggregates often consisted of hobnail-shaped cells organized around either clear-cell or hyalinized cores (Fig. 4I). OSE hyperplasia and small clumps of hobnail cells were evident on the ovarian surface as early as one week following AdCRE injection, with exfoliated tumor cell aggregates and clear-cell-like features apparent at 2 weeks (Supplementary Fig. 3). The tumors were also positive for the human OCCC marker, HNF1β, by IHC (Fig. 5B).

Thus, mouse ovarian tumors harboring coexistent *ARID1A-PIK3CA* mutations share histopathological features with human OCCC.

Tumor gene expression supports a role for IL-6 in OCCC

To further evaluate the relevance of our *Arid1a*$^{fl/fl}$*;(Gt)Rosa26Pik3ca*^{*H1047R} ovarian tumor model to human OCCC, we performed a series of cross-species gene expression comparisons using a well-characterized gene expression dataset containing all four human EOC subtypes[39]. Gene expression profiles of mouse primary tumor samples and matched normal (uninjected) ovaries were generated by microarray. Consistent with our genetic model, ARID1A and PIK3CA expression levels were inversely correlated in comparisons between tumor and normal ovary samples, with PIK3CA upregulation strongly correlated with ARID1A downregulation in the tumor samples (Supplementary Fig. 4). We verified our microarray gene expression results by RT-PCR validation of KRAS, TFPI2, CDKN2A (P16), CDKN1A (P21), MUC16 (CA125), and VCAN expression (Supplementary Fig. 5). We next identified all coordinately regulated genes in both mouse tumors and human OCCC, as compared to species-matched normal ovaries. In comparisons of both mouse and human datasets, the control ovary samples showed high levels of gene expression variation, suggesting tissue sampling differences or general interspecies-specific gene expression differences (Supplementary Fig. 6). Focusing on those genes that remained unchanged in normal mouse and human ovaries, we identified 584 coordinately regulated genes (272 upregulated; 312 downregulated) in mouse and human tumors (Supplementary Fig. 7). Mouse and human tumor gene expression patterns were enriched for genes involved in Interleukin-6 (IL-6) signaling, immune system function, focal adhesion, and regulation of the actin cytoskeleton, as compared to normal ovaries (Supplementary Figs. 6 and 7).

Since many of the upregulated genes we identified in cross-species comparisons with normal ovaries are likely to be found in other EOC subtypes (e.g. CA125) or generally found across most cancers, we next sought to identify an OCCC-specific gene signature for use in subtype-specific gene expression comparisons with the mouse tumors. To do this, we compiled a more refined ‘discriminant’ gene list for each subtype (e.g. clear-cell vs. all other EOC subtypes). We then compared the normalized raw expression values for each discriminant gene across all of the mouse tumor and human EOC samples. Using this analysis, we found that the gene expression patterns for mouse tumor and human OCCC samples were not statistically different (pval=0.6), suggesting that the OCCC-specific gene expression patterns are conserved between the two species (Fig. 5C). Several well-known markers of OCCC were identified as being highly expressed in the mouse tumors, including IL-6, STAT3, VCAN, and HIF1α, further supporting a role for heightened IL-6 signaling in OCCC tumor pathogenesis[40, 41, 42] (Fig. 6A).

To further assess similarities between our genetic model and human OCCC, we compared the mouse tumor-specific gene expression profiles for our *Arid1a*$^{fl/fl}$*;(Gt)Rosa26Pik3ca*^{*H1047R} mouse model to those recently reported for the *Arid1a*$^{fl/fl}$; *Pten*$^{fl/fl}$ mouse model by Guan *et al*.[26], which is genetically similar endometrioid EOC. Both models relied on the intrabursal AdCRE injection method for mutation induction. We applied principal component analysis using the normalized expression values for all genes in the

tumor datasets for each mouse model. We found that each tumor sample clustered based on genotype or mutational pattern of the respective genetic model, with the exception of one *Arid1a*$^{fl/fl}$; *Pten*$^{fl/fl}$ tumor (Supplementary Fig. 8). These findings are consistent with the marked phenotypic differences observed in our *Arid1a*$^{fl/fl}$*;(Gt)Rosa26Pik3ca*^{*H1047R} tumors when compared to the phenotypes reported for *Arid1a*$^{fl/fl}$; *Pten*$^{fl/fl}$ tumors by Guan *et al.*[26].

Autocrine IL-6 signaling promotes tumor cell growth

IL-6 is an inflammatory cytokine that triggers JAK/STAT3 signaling and has prominent roles in tumor cell growth and differentiation[43, 44]. High levels of circulating IL-6 in cancer patients are associated with a poor prognosis[43, 44]. In addition to its increased expression in OCCC tumors, IL-6 has been detected in patient serum and tumor-derived cell lines, which has led to its proposed use as a therapeutic target in OCCC[40, 41, 42]. In support of our cross-species microarray comparisons, we verified IL-6 expression in primary tumors and peritoneal metastases of *Arid1a*$^{fl/fl}$*;(Gt)Rosa26Pik3ca*^{*H1047R} mice by RT-PCR (Fig. 6B). We also observed high levels of secreted IL-6 in the body fluids of tumor-burdened mice, with greater than 2000 pg/mL of IL-6 in ascitic fluid aspirates (Fig. 6C,D). Consistent with this, strong IL-6 immunoreactivity was also observed in the mouse tumors by IHC (Fig. 6E).

To understand the role of IL-6 in OCCC pathogenesis, we treated primary *Arid1a*$^{fl/fl}$*;(Gt)Rosa26Pik3ca*^{*H1047R} mouse ascites-derived tumor cells, isolated as described above, with anti-IL-6 neutralizing antibodies. Anti-IL-6 treatment reduced tumor cell viability and downregulated phosphorylation of STAT3 at tyrosine 705 (P-STAT3 Y705), suggesting that autocrine IL-6-STAT3 signaling promotes tumor cell growth (Fig. 6F,G). Next, we generated primary mouse tumor cell lines that stably express IL-6 short-hairpin RNAs (shRNA) for use in tumor growth assays (Fig. 6H,I). IL-6 shRNA-expressing cells showed reduced growth rates in culture, and media supplementation with recombinant IL-6 restored the normal growth patterns of IL-6 shRNA-expressing cells (Fig 6J). To further examine tumor cell autonomous roles for IL-6 in ovarian tumor cell growth, we grafted control shRNA- and IL-6 shRNA-expressing mouse tumor cells onto the flanks of immunodeficient nude mice. Remarkably, the ascitic tumor cell grafts were indistinguishable from the ovarian tumors with regards to histopathological features (e.g clear cytoplasm), despite being maintained in tissue culture and further grown under the skin of immunodeficient mice (Fig. 6K,L). The rate of tumorgraft growth for IL-6 shRNA-expressing cells was significantly less than control shRNA-expressing cells, further indicating that autocrine IL-6 signaling contributes to OCCC pathogenesis by promoting tumor cell growth (Fig. 6M).

IL-6 induction requires coexistent *ARID1A-PIK3CA* mutations

To determine if coexistent *ARID1A-PIK3CA* mutations are required for IL-6 induction, we utilized an AdCRE-inducible primary OSE cell culture model. IL-6 expression was measured following AdCRE-infection of primary OSE cells isolated from mice carrying all mutant allele combinations. Loss of ARID1A or PIK3CA activation alone led to significant increases in IL-6 expression by RT-PCR and ELISA, and IL-6 induction was further enhanced when *ARID1A* and *PIK3CA* were co-mutated together in *Arid1a*$^{fl/fl}$*;(Gt)Rosa26Pik3ca*^{*H1047R} cells (Fig. 7A,B). Consistent with this, P-STAT3 Y705 levels also correlated with similar increases in IL-6 activity in AdCRE treated OSE cells (Fig. 7C).

ARID1A loss in AdCRE-treated *Arid1a*$^{fl/fl}$ or *Arid1a*$^{fl/fl}$*;(Gt)Rosa26Pik3ca*^{*H1047R} OSE cells did not further enhance PI3K pathway activity (Fig. 7C). We found that *Arid1a*$^{fl/fl}$*; (Gt)Rosa26Pik3ca*^{*H1047R} OSE cell proliferation was suppressed by treatment with anti-IL-6 neutralizing antibodies following mutation induction with AdCRE, and that recombiant IL-6 enhances normal OSE cell proliferation and IL-6-STAT3 signaling, further suggesting that IL-6 is both necessary and sufficient for tumor cell growth (Fig 7D–F). To determine if ARID1A is bound at the *IL6* promoter under repressed conditions, we performed a series of ARID1A chromatin immunoprecipitation experiments in primary OSE cells. We used *Arid1a*$^{fl/fl}$*;(Gt)Rosa26Pik3ca*^{*H1047R} OSE cells for these experiments so that AdCRE-treated or ARID1A-depleted cells could be used as a control for ARID1A immunoprecipitation specificity. In AdControl-treated cells, increased ARID1A occupancy was observed at sites near the *IL6* promoter, but not at distal upstream or downstream sites (Fig. 7G). ARID1A occupancy at this site decreased in manner consistent with ARID1A depletion following AdCRE infection. These data indicate that coexistent *ARID1A-PIK3CA* mutations lead to IL-6 upregulation.

Discussion

Our data support a genetic epistasis model wherein *ARID1A* and *PIK3CA* mutations cooperate and ovarian cancer can arise only when these genes are co-mutated in the mouse OSE. The short latency period, lack of copy number variation, and OCCC-like histological and molecular features we observed are also consistent with coexistent *ARID1A-PIK3CA* mutations being a major driver of OCCC in humans. Our results suggest that high levels of tumor cell-derived IL-6 are promoting tumor growth in OCCC. Indeed, the top pathway we identified in common between species is comprised of genes involved in this pathway, suggesting that IL-6-STAT3 signaling is inherent to OCCC biology. Hence, IL-6 serves as both a molecular marker and a prospective therapeutic target in OCCC. Therefore, anti-IL-6 antibody (*Siltuximab*) therapy may prove to be a safe and effective treatment strategy for OCCC patients. More broadly, our findings further demonstrate that the continued identification of tumor mutations (i.e. TCGA projects) will allow us to identify potential functional relationships among recurrent mutational patterns or cancer pathways that would have otherwise gone unnoticed.

The OSE-derived tumor phenotypes we observed in our *Arid1a*$^{fl/fl}$*; (Gt)Rosa26Pik3ca*^{*H1047R} mouse model of OCCC greatly contrasted with those reported by Guan *et al*.[26] for *Arid1a*$^{fl/fl}$; *Pten*$^{fl/fl}$ mice. For example, all of the tumor-burdened *Arid1a*$^{fl/fl}$*; (Gt)Rosa26Pik3ca*^{*H1047R} mice were morbid or succumbed to death within 3 months after AdCRE injection, whereas Guan *et al*.[26] reported tumors in a subset of *Arid1a*$^{fl/fl}$; *Pten*$^{fl/fl}$ mice after 6 months, indicating stark differences in tumor latency or survival. Molecular differences were evident in tumor gene expression comparisons between the two mouse models, as each gene expression dataset parsed the majority of tumor samples based on its respective mutational pattern or genotype. These data point to potential functional differences between *ARID1A-PIK3CA* and *ARID1A-PTEN* mutational patterns in Type I EOCs and support the idea of a possible PI3K-AKT-mTOR-independent role for PTEN in endometrioid EOC[26]. Alternatively, it remains possible that clear-cell tumorigenesis is driven, in part, by an alternative AKT-independent mechanism downstream of oncogenic

PIK3CA mutations[45, 46]. Additional pharmacological studies targeting downstream effectors or alternative signaling pathway components will further address potential PI3K pathway-independent mechanisms of endometrioid versus clear-cell tumorigenesis.

Several theories on the origins of OCCC have been proposed. Our data strongly suggests that the OSE harbors a cancer-prone cell population that gives rise to OCCC-like tumors in the mouse, which is consistent with the classical view of EOC pathogenesis. Nonetheless, our mouse model does not address the role of distal endometriotic explants or other putative precursor lesions in OCCC pathogenesis. Specifically targeting the *ARID1A-PIK3CA* mutational pattern to other tumor-prone epithelia within the Müllerian duct system would add relevance to our findings and help to further clarify the origins of EOC. An improved set of inducible CRE alleles would facilitate these experiments.

Inflammation of coelomic epithelial cell-derivatives in the female reproductive tract is thought to be a major contributor to malignant transformation in endometriosis-associated EOC, like OCCC[5, 47]. Accordingly, inflammatory mediators, aberrant immune modulation, or irregular reproductive hormone levels are thought to play a major role in malignant transformation[5, 47]. Inflammatory cytokine signaling pathways, like IL-6, may be part of the natural inflammatory repair process accompanying each ovarian and menstrual cycle that, when left unchecked, promotes unregulated epithelial cell growth. In support of this, our data demonstrate that OSE cells are competent to respond to and upregulate IL-6. Therefore, the incomplete resolution of epithelial cell inflammation during these repair processes may represent a common mechanism underlying OCCC tumorigenesis, irrespective of mutational pattern.

The identification of IL-6 as a physiological target of ARID1A tumor suppressor activity in our OCCC tumor model raises many important questions regarding the role of ARID1A-containing SWI/SNF complexes in normal coelomic epithelial cell homeostasis. Indeed, ARID1A mutations have been identified in a wide variety of cancers originating from coelomic epithelial-derivatives throughout the gynecologic tract. Moreover, loss of ARID1A immunoreactivity is observed in endometriosis, a disease intimately associated with inflammation[48, 49, 50]. Endometriosis is also characterized by increased IL-6 expression, but the relationship between ARID1A loss and IL-6 upregulation in endometrial tissue is unknown[51, 52]. Thus, ARID1A may regulate coelomic epithelial cell homeostasis and prevent tumorigenic conversion by negatively regulating the inflammatory programs required for normal tissue repair during the female reproductive cycle. It will be interesting to know if reproductive hormones influence ARID1A activity in this regard. Additional work on the propensity of *ARID1A* mutant epithelial cells to undergo malignant transformation in response to inflammatory “insults” or the role of key inflammatory response pathways in this process will be required to address these hypotheses. Thus, loss of ARID1A-containing SWI/SNF complexes might expose the “darker,” pro-tumorigenic side of inflammation.

How do oncogenic PI3K signaling mutations contribute to this process or lead to increased IL-6 expression? Positive regulators of IL-6 include JAK/STAT, PI3K, EGFR/HER2, RAS/RAF/MEK, TNF/TLR/IL1 or RAS/ERK oncogenic pathways and AP-1, SP1, NF-κB,

C/EBP, STAT3, and CREB transcription factors[53]. IL-6-mediated JAK/STAT activation can further promote IL-6 transcription[53]. We propose that oncogenic *PIK3CA*^{H1047R} mutations act like inflammatory "insults" and drive the signaling loop that sustains high levels of IL-6 production in the absence of negative regulation by ARID1A (Fig 7H). Additional studies focusing on the intricacies of this feed-forward signaling loop and the potential crosstalk mechanisms occurring among the various pathways that sustain it will further explain why coexistent *ARID1A-PIK3CA* mutations are found in a wide variety of human cancers.

Material and Methods

Generation of the *Arid1a* conditional mouse allele

The *Arid1a*^{fl} conditional mutant mouse allele was engineered using the Bacterial Artificial Chromosome (BAC) recombineering methods developed by Liu *et al*[54]. Correctly targeted mouse ES cell clones were identified by Southern blotting. The *Neo* selection cassette used for targeting was removed by FLP-mediated recombination[54]. Targeted ES cells were injected into C57Bl6 blastocysts and implanted into pseudopregnant females. Germline animals were detected by coat color and PCR confirmation of tail DNA samples.

AdCRE-mediated genetic recombination in the ovary

To induce genetic recombination in the ovarian surface epithelium (OSE), we employed a modified version of the *ex-vivo* Adenovirus-CRE (AdCRE) intrabursal delivery method[7, 29]. Briefly, AdCRE particles (obtained from the University of Iowa Gene Transfer Core) were diluted in sterile 1X Dulbeccos's phosphate buffered saline (dPBS) containing 8 μg/mL polybrene. Deeply anesthetized 8–10 week old mice were given a single 5 μL injection of AdCRE particles (2.5×10^7 plaque-forming units or pfu) into the right ovarian bursal cavity of the surgically exposed ovary using a sterile 31-gauge needle. Immediately following AdCRE injection, the surgically excised ovaries were washed with sterile 1X dPBS and placed back into the abdominal cavity. The surgeries were performed on multiple occasions. Age- and genotype-matched, non-littermate animals were randomized prior to AdCRE injection. The surgeon was blinded to the genotypes prior to surgery and AdCRE injection. All surgical procedures were performed in accordance with protocols approved by the University of North Carolina at Chapel Hill Institutional Animal Care and Use Committee.

Mouse husbandry and genotyping

All mice were maintained on an outbred (random) genetic background using CD-1 mice (Charles River). *(Gt)ROSA26*^{Pik3ca*H1047R} and *Sox2CRE* alleles were purchased from The Jackson Laboratory and identified by PCR using published methods[28, 35]. *Arid1a*$^{+/+}$; *Arid1a*$^{fl/+}$; *Arid1a*$^{fl/fl}$ alleles were distinguished by PCR using the following primer set: (F) CTAGGTGGAAGGTAGCTGACTGA; (R) TACACGGAGTCAGGCTGAGC. Combining the forward primer (from above) with the following reverse primer amplifies the CRE-excised allele: (R) AGAGTAACTAATAACTGCTGGAGGATG. PCR products were resolved by 2%–Tris-Borate-EDTA agarose gel electrophoresis. Endpoints were palpable tumors (>1.5 cm^3), visible hemorrhagic ascites or severe abdominal distension, and signs of severe illness, such as dehydration, hunching, ruffled fur, signs of infection, or non-responsiveness. Sample sizes within each genotype were chosen based on the proportions of

animals with tumors and/or survival between each experimental group or a Kaplan-Meyer log rank test for survival differences. Wholemount live animal luminescent imaging was performed using the IVIS Optical System and reagents (Perkin Elmer) according to the manufacturer's instructions. Wholemount images of mice or necropsies were aquired using a Canon PowerShot SD1100 IS digital camera and a tabletop tripod. Wholemount tumor specimens were imaged on a Leica MZ FLIII stereomicroscope using a DS Ri1 digital camera (Nikon). All mice were maintained at the University of North Carolina at Chapel Hill, Animal Facility using standard techniques in accordance with protocols approved by the University of North Carolina at Chapel Hill Institutional Animal Care and Use Committee.

In vivo drug treatments

The pan-PI3K inhibitor, BKM120 (Novartis) was milled by Research Diets using a vehicle- or carrier-free formulation similar to standard husbandry diets and dosed at 40 mg kg^{-1} based on the average daily oral consumption of a mouse[55, 56, 57]. AdCRE-injected animals were randomized prior to drug treatment. Control or untreated mice were given a standard husbandry diet. All drug treatments were performed in accordance with protocols approved by the University of North Carolina at Chapel Hill Institutional Animal Care and Use Committee.

RT-PCR

Total RNA was extracted from pulverized tumor samples or ovarian epithelial cells using the TRIzol method (Invitrogen), followed by an RNA cleanup step and on-column DNA digestion using the RNAeasy mini prep kit (Qiagen) according to the manufacturers' instructions. To analyze *ARID1A* and *(Gt)Rosa26*^{Pik3ca*H1047R} gene transcript levels, real-time quantitative PCR was performed using Ssofast PCR master mix (Biorad) and a CFX96 thermocycler (Biorad) with the following gene-specific primers: ARID1A (F) CTGAAGGACAAAGGTGACT, ARID1A (R) CACAACTGCGAACTTCTC; R26exon1 (F) CTAGGTAGGGGATCGGGACTCT, PIK3CAcDNA (R) AATTTCTCGATTGAGGATCTTTTCT[35]. The following gene specific primers were used to validate the microarray expression data: KRAS (F) AGAGGAGTACAGTGCAATGAGG, KRAS (R) AGGCACATCTTCAGAGTCCTTT; TFPI2 (F) AAGGGCTTGTGTGAACCACG, (R) CCACCACAGCCAGTATAGGTG; CDKN1A (F) ATCCAGACATTCAGAGCCACAG, (R) ACGAAGTCAAAGTTCCACCGT; CDKN2A (F) GCTTCTCACCTCGCTTGTCA, (R) AGTGACCAAGAACCTGCGAC; MUC16 (F) CTCATCTGCTTGGCGGTACT; (R) GAACCCTGCTAGGGAAGAGC; VCAN (F) GAAGGGAACAGTTGCTTGCG, (R) TTAGGCATTGCCCATCTCCC; IL-6 (F) CACTTCACAAGTCGGAGGCT, (R) CTGCAAGTGCATCATCGTTGT. Expression was calculated from three independent experiments using $\Delta\Delta C_t$ methods. Expression levels were normalized to *βACTIN*. Statistical differences were detected using a two-tailed Student's *t* test. The following H1047 spanning PCR primer pair was used to distinguish endogenous *PIK3CA* from *Rosa26*-derived, *PIK3CA*^{H1047R} gene transcripts: (F) TTCAATGATGCTTGGCTCTG; (R) CTGCTTGATGGTGTGGAAGA. The PCR products were digested with MslI and resolved by 2%–Tris-Borate-EDTA agarose gel electrophoresis.

Western blotting

Western blots were performed using the following antibody dilutions and standard chemiluminescent detection methods or Li-COR Bioscience Odyssey fluorescent western blotting reagents: 1:1,000 ARID1A (A301-041A, Bethyl Labs,), 1:500 IL-6 (ab6672, Abcam), 1:1000 Phospho-AKT Ser473 (4060, Cell Signaling), 1:1000 AKT (4691, Cell Signaling), 1:100 STAT3 (sc-482, Santa Cruz Biotechnology), 1:1000 Phospho-STAT3 Tyr705 (9145, Cell Signaling), and 1:5,000 βACTIN (Abcam). Membranes were blocked in 1X PBS supplemented with 5% (w/v) non-fat dry milk (Blotto A) or 1X Tris-buffered saline (TBS) [pH 7.6] supplemented with 5% (w/v) bovine serum albumin (BSA). Primary antibody incubations were performed in 1X PBS supplemented with 1% (w/v) non-fat dry milk, 1% (w/v) BSA, and 0.05% (v/v) Tween-20 (Blotto B) or 1X TBS [pH 7.6] supplemented with 5% (w/v) BSA. Western blot images have been cropped for presentation. Full size western blot images with antibody dilutions and blocking buffer conditions are presented in Supplementary Figures 9 and 10.

ELISA

IL-6 ELISAs were performed using the OptEIA mouse IL-6 kit reagents (BD Bioscience) according to the manufacturer's instructions. ELISA measurements were normalized to total cellular protein.

Copy number and TCGA computational analyses

Tumor and matched control DNA samples were processed for hybridization on the high density Mouse Universal Genotyping SNP Array (MegaMUGA, Neogen) using published methods[58]. Copy number analysis was performed using ASCAT[59]. ARID1A and/or PIK3CA TCGA mutation frequency was identified by querying the cBioPortal on 2014-10–21 using the R API [60, 61].

Microarray and cross-species gene expression comparisons

Total RNA was isolated from 9 primary tumor specimens and 9 matched normal (uninjected) ovaries as described above. Total RNA (250 ng) was used to synthesize fragmented and labeled sense-strand cDNA and hybridize onto Affymetrix Mouse Gene 2.1 ST peg plate arrays. The mouse data were uploaded to the Gene Expression Omnibus (GEO) under the accession number: GSE57380. Affymetrix CEL files were normalized using the Robust Multichip Average normalization method[62]. Expression changes (tumor versus control ovary) were determined using Linear Models for Microarray Data Analysis (LIMMA)[63] or Significance Analysis of Microarray (SAM) analysis[64]. Probes with a false discovery rate (FDR) of 0% were considered statistically significant. For mouse-human cross species comparisons, expression data for human OCCC and normal ovaries were downloaded from GEO under the accession number GSE6008[39]. Heat maps and dendrograms were generated with Java TreeView or R (www.R-project.org). Histological sub-type specific gene signatures were derived by first identifying differentially expressed genes between human normal tissue and cancer tissue in GSE6008. Next, differentially expressed genes were identified comparing each histological subtype to all other histological subtypes. We considered only upregulated genes, and any genes that were upregulated in

both the tumor versus normal comparison and in a particular subtype were removed because these are not specific to a histological subtype and may reflect generic pan-cancer gene expression patterns. To compare human and mouse samples from these gene sets we first determined Z-scores for each gene within mouse or human. We combined these Z-scores and Z-scored the combined data using all human and mouse tumor samples in GSE6008 and this study. Pathways analysis was perfomed using the GSEA Molecular Signatures Database (MSigDB)[65, 66] or Ingenuity Pathway Analysis (IPA) (Qiagen).

Ascites-derived tumor cell and OSE cell culture

Primary ascites-derived ovarian tumor cells were isolated and grown as previously described[67]. To facilitate complete red blood cell lysis, the cell isolates were incubated and washed in deionized H_2O prior to re-suspension in growth medium. Mouse OSE cells were isolated and cultured as previously described[68]. To induce CRE-mediated recombination in OSE cells, the cells were infected with AdCRE or AdControl particles (obtained from the University of Iowa Gene Transfer Core) at an MOI of 200 for 2 hours in serum-free media. Infected OSE cells were then placed in normal growth medium and allowed to recover for 3 days prior to further manipulation. BKM120 (Chemitek), low endotoxin rat anti-mouse IL-6 neutralization antibody (R&D systems, MAB406), non-specific rat IgG_1 isotype control antibody (R&D systems, MAB005), or recombinant mouse IL-6 protein (R&D systems, 406-ML-005) were reconstituted according to the manufacturers' instructions and used as described in the text. For all antibody neutralization experiments, the cells were re-fed daily with the appropriate concentrations of antibody. Primary ascites-derived ovarian tumor cells were stably transduced with Mission pLKO.1-puro IL-6 shRNA (Hairpin sequence: CCGGCCAGAGTCCTTCAGAGAGATACTCGAGTATCTCTCTGAAGGACTCTGGTTTTTG) (Sigma, TRCN0000067551) or non-target control shRNA (Sigma, SHC016V) Lentiviral transduction particles according to the manufacturers' instructions. The MTT assay kit (Roche) was used to measure cell viability. Ascites-derived tumor cells and OSE cells were passaged using Accutase (Invitrogen). Half-maximal inhibitory concentrations (IC_{50}) were calculated by curve-fitting using Kaleidagraph software (Synergy).

Tumor grafts

Primary ascites-derived ovarian tumor cells expressing control- or IL-6 shRNAs were harvested by Accutase digestion and washed in 1X Dulbecco's phosphate buffered saline. The cells were then injected subcutaneously into the right flanks of immunodeficient mice at a concentration of 5×10e7 cells/mL in a 1:1 (v/v) solution of 1X Dulbecco's phosphate buffered saline and Cultrex basement membrane extract (3432-005-01, Trevigen). Tumor graft volumes were calculated using bi-weekly caliper-based measurements and growth rates were based on these volumetric measurements. All tumor grafts were performed in accordance with protocols approved by the University of North Carolina at Chapel Hill Institutional Animal Care and Use Committee.

Histology and immunohistochemistry

For indirect immunohistochemistry of slides, 10% neutral buffered formalin-fixed paraffin sections were processed for heat-based antigen unmasking in 10 mM sodium citrate [pH 6.0]. Sections were incubated with the following antibody dilutions: 1:50 ARID1A (Clone

PSG3, sc-32761, Santa Cruz Biotechnology), 1:100 Cytokeratin 8 (TROMAI, DSHB), 1:50 phospho-AKT Ser473 (4060, Cell Signaling), 1:50 phospho-S6 Ribosomal Protein Ser235/236 (4858, Cell Signaling), 1:100 HNF1β (sc-7411, Santa Cruz Biotechnology), or 1:400 IL-6 (ab6672, Abcam). Vectastain Mouse-on-Mouse blocking reagents (Vector Labs) were used for ARID1A immunohistochemistry. SignalStain antibody diluent (8112, Cell Signaling) and SignalSlide AKT controls (8115, Cell Signaling) were used for phospho-AKT Ser473 and phospho-S6 Ribosomal Protein Ser235/236 immunohistochemistry. Secondary detection was performed using Vectastain ABC System reagents (Vector Labs). Sections processed for immunohistochemistry were lightly counter-stained with Hematoxylin QS or Methyl Green (Vector Labs). Routine Hematoxylin and Eosin (H&E) staining of sections was perfomed by University of North Carolina, Lineberger Cancer Center, Animal Histopathology Core. Histological tumor assessments were reviewed by a UNC animal pathologist. Histological sections were analyzed and photographed on an Olympus BX51 microscope using bright-field optics and a DP series digital camera (Olympus).

Chromatin immunoprecipitation

Primary OSE cells were fixed in growth media containing 1% methanol-free formaldehyde (Pierce) for 10 min. at room temperature. The cells were washed twice with 1X dPBS and then swelled in cell lysis buffer (5 mM Tris-Cl [pH 8.0]; 85 mM KCl; 1% IGEPAL CA-630) for 10 min. on ice. Swollen cells were homogenized (20 strokes) with a B-type dounce homogenizer on ice to facilitate nuclei release. Isolated nuclei corresponding to 1×10e7 cell equivalents per 500 μL of nuclear lysis buffer (50 mM Tris-Cl [pH 8.0], 10 mM EDTA, and 0.3% SDS) and then sonicated using a water bath-cooled Diagenode Biorupter sonicator and 1.5 mL TPX microtubes (200 μL sample volume per tube) to an average DNA length between 300 and 700 bp. Chromatin concentrations were determined using a BCA protein assay kit (Pierce). Chromatin samples were diluted to 300 μg per 200 μL of nuclear lysis buffer and then cleared by centrifugation at 10,000Xg. Pre-cleared chromatin samples (200 μL each) were added to 800 μL (1:5 dilution) of ChIP dilution buffer (50 mM Tris-Cl [pH 7.5]; 150 mM NaCl; 5 mM EDTA; 0.5% IGEPAL CA-630; 1% TX-100) and incubated with 10 μg of prebound ARID1A (Clone PSG3, 04-080, Millipore) Protein G dynal beads (Invitrogen) overnight at 4°C. The Protein G dynal bead-anti-ARID1A immune conjugates were washed twice with 1 mL ChIP dilution buffer, 3-times with 1 mL ChIP dilution buffer supplemented with 500 mM NaCl, twice with 1 mL ChIP dilution buffer, followed by a final wash in 1 mL low salt TE buffer (10 mM Tris-Cl [pH 8.0]; 1 mM EDTA; 50 mM NaCl). The immunoprecipitated samples were eluted in 100 μL of elution buffer (50 mM $NaHCO_3$; 1% SDS) at 62°C for 20 min. using an Eppendorf tube mixer. The crosslinks were reversed by adding NaCl to a final concentration of 0.2M followed by an overnight incubation at 65°C. The samples were then deproteinated with Proteinase K and purified using the ChIP DNA Clean & Concentrator kit (Zymo Research) according to the manufacturer's instructions. Real-time quantitative PCR using Ssofast PCR master mix (Biorad) and a CFX96 thermocycler (Biorad) was performed using the following gene-specific primer pairs: (IL-6, Site A) GCAACTCTCACAGAGACTAAAGG, GGACAACAGACAGTAATGTTGC[69]; (IL-6, Site B) CTAGCCTCAAGGATGACTTAAGC, CTATCGTTCTTGGTGGGCTCCAGAGC[70];

(IL-6, Site C) GCCTTCTTGGGACTGATGCT, GACAGGTCTGTTGGGAGTGG. Data from three independent primary OSE cell isolations were averaged and plotted as a percentage of the total input.

Supplementary Material

Refer to Web version on PubMed Central for supplementary material.

Acknowledgements

We thank members of the Magnuson and Kim Lab and Drs. Scott Bultman and Victoria Bae-Jump for helpful discussions. We thank Dr. Anna Spagnoli for generously sharing imaging equipment, Jane Hoel and Jackie Brooks for help with the AdCRE injections, Mike Vernon for performing the microarray hybridizations, and members of the Laboratory of Pardo-Manuel de Villena for technical assistance with the copy number analysis. We also thank Drs. Susan Murphy and Zhiqing Huang at Duke for their helpful discussions on primary ovarian tumor cell isolation methods. Dr. Virginia Godfrey at UNC provided assistance with mouse tumor pathology. The UNC Lineberger Comprehensive Cancer Center's Mouse Phase One Unit (MP1U) provided assistance with the therapeutic studies. MP1U is supported by the University Cancer Research Fund. R.L.C. was supported by an American Cancer Society Postdoctoral Fellowship (PF-09-116-01-CCG) and an Ann Schreiber Mentored Investigator Award (258831) from the Ovarian Cancer Research Fund. J.S.D was supported by the Integrative Vascular Biology Training Grant (T32-HL069768). W.Y.K is a Damon Runyon Merck Clinical Investigator. This work was supported by an AACR Kurelt grant to W.Y.K. and NIH grants to W.Y.K (CA142794) and T.M. (HD03665).

References

1. Siegel R, Naishadham D, Jemal A. Cancer statistics, 2013. CA: a cancer journal for clinicians. 2013; 63:11–30. [PubMed: 23335087]
2. Adashi, EY.; Leung, PCK. The Ovary. Raven Press; 1993.
3. Perets R, et al. Transformation of the fallopian tube secretory epithelium leads to high-grade serous ovarian cancer in Brca;Tp53;Pten models. Cancer Cell. 2013; 24:751–765. [PubMed: 24332043]
4. Vigano P, Somigliana E, Chiodo I, Abbiati A, Vercellini P. Molecular mechanisms and biological plausibility underlying the malignant transformation of endometriosis: a critical analysis. Human reproduction update. 2006; 12:77–89. [PubMed: 16172112]
5. Ness RB. Endometriosis and ovarian cancer: thoughts on shared pathophysiology. Am J Obstet Gynecol. 2003; 189:280–294. [PubMed: 12861175]
6. Kurman RJ, Shih Ie M. The origin and pathogenesis of epithelial ovarian cancer: a proposed unifying theory. The American journal of surgical pathology. 2010; 34:433–443. [PubMed: 20154587]
7. Dinulescu DM, Ince TA, Quade BJ, Shafer SA, Crowley D, Jacks T. Role of K-ras and Pten in the development of mouse models of endometriosis and endometrioid ovarian cancer. Nat Med. 2005; 11:63–70. [PubMed: 15619626]
8. Wu R, et al. Mouse model of human ovarian endometrioid adenocarcinoma based on somatic defects in the Wnt/beta-catenin and PI3K/Pten signaling pathways. Cancer Cell. 2007; 11:321–333. [PubMed: 17418409]
9. Glasspool RM, McNeish IA. Clear cell carcinoma of ovary and uterus. Curr Oncol Rep. 2013; 15:566–572. [PubMed: 24114188]
10. Cho KR, Shih Ie M. Ovarian cancer. Annu Rev Pathol. 2009; 4:287–313. [PubMed: 18842102]
11. Tan DS, Miller RE, Kaye SB. New perspectives on molecular targeted therapy in ovarian clear cell carcinoma. Br J Cancer. 2013; 108:1553–1559. [PubMed: 23558892]
12. Kobayashi H. Ovarian cancer in endometriosis: epidemiology, natural history, and clinical diagnosis. Int J Clin Oncol. 2009; 14:378–382. [PubMed: 19856043]
13. Jimbo H, Yoshikawa H, Onda T, Yasugi T, Sakamoto A, Taketani Y. Prevalence of ovarian endometriosis in epithelial ovarian cancer. Int J Gynaecol Obstet. 1997; 59:245–250. [PubMed: 9486515]

14. Ness RB. Endometriosis and ovarian cancer: thoughts on shared pathophysiology. American journal of obstetrics and gynecology. 2003; 189:280–294. [PubMed: 12861175]
15. Itamochi H, Kigawa J, Terakawa N. Mechanisms of chemoresistance and poor prognosis in ovarian clear cell carcinoma. Cancer Sci. 2008; 99:653–658. [PubMed: 18377417]
16. Tan DS, Kaye S. Ovarian clear cell adenocarcinoma: a continuing enigma. J Clin Pathol. 2007; 60:355–360. [PubMed: 17018684]
17. Jones S, et al. Frequent mutations of chromatin remodeling gene ARID1A in ovarian clear cell carcinoma. Science. 2010; 330:228–231. [PubMed: 20826764]
18. Wiegand KC, et al. ARID1A mutations in endometriosis-associated ovarian carcinomas. The New England journal of medicine. 2010; 363:1532–1543. [PubMed: 20942669]
19. Wu JN, Roberts CW. ARID1A mutations in cancer: another epigenetic tumor suppressor? Cancer Discov. 2013; 3:35–43. [PubMed: 23208470]
20. Jones S, et al. Genomic analyses of gynaecologic carcinosarcomas reveal frequent mutations in chromatin remodelling genes. Nature communications. 2014; 5:5006.
21. Kadoch C, et al. Proteomic and bioinformatic analysis of mammalian SWI/SNF complexes identifies extensive roles in human malignancy. Nature genetics. 2013; 45:592–601. [PubMed: 23644491]
22. Wang X, Haswell JR, Roberts CW. Molecular Pathways: SWI/SNF (BAF) complexes are frequently mutated in cancer-mechanisms and potential therapeutic insights. Clinical cancer research : an official journal of the American Association for Cancer Research. 2013
23. Jones S, et al. Somatic mutations in the chromatin remodeling gene ARID1A occur in several tumor types. Hum Mutat. 2012; 33:100–103. [PubMed: 22009941]
24. Chandler RL, Brennan J, Schisler JC, Serber D, Patterson C, Magnuson T. ARID1a-DNA interactions are required for promoter occupancy by SWI/SNF. Molecular and cellular biology. 2013; 33:265–280. [PubMed: 23129809]
25. Lengyel E, et al. Epithelial ovarian cancer experimental models. Oncogene. 2014; 33:3619–3633. [PubMed: 23934194]
26. Guan B, et al. Roles of deletion of Arid1a, a tumor suppressor, in mouse ovarian tumorigenesis. Journal of the National Cancer Institute. 2014; 106
27. Gao X, Tate P, Hu P, Tjian R, Skarnes WC, Wang Z. ES cell pluripotency and germ-layer formation require the SWI/SNF chromatin remodeling component BAF250a. Proc Natl Acad Sci U S A. 2008; 105:6656–6661. [PubMed: 18448678]
28. Hayashi S, Lewis P, Pevny L, McMahon AP. Efficient gene modulation in mouse epiblast using a Sox2Cre transgenic mouse strain. Mech Dev. 2002; 1(119 Suppl):S97–S101. [PubMed: 14516668]
29. Flesken-Nikitin A, Choi KC, Eng JP, Shmidt EN, Nikitin AY. Induction of carcinogenesis by concurrent inactivation of p53 and Rb1 in the mouse ovarian surface epithelium. Cancer Res. 2003; 63:3459–3463. [PubMed: 12839925]
30. Campbell IG, et al. Mutation of the PIK3CA gene in ovarian and breast cancer. Cancer research. 2004; 64:7678–7681. [PubMed: 15520168]
31. Kuo KT, et al. Frequent activating mutations of PIK3CA in ovarian clear cell carcinoma. Am J Pathol. 2009; 174:1597–1601. [PubMed: 19349352]
32. Zang ZJ, et al. Exome sequencing of gastric adenocarcinoma identifies recurrent somatic mutations in cell adhesion and chromatin remodeling genes. Nature genetics. 2012; 44:570–574. [PubMed: 22484628]
33. Yamamoto S, Tsuda H, Takano M, Tamai S, Matsubara O. Loss of ARID1A protein expression occurs as an early event in ovarian clear-cell carcinoma development and frequently coexists with PIK3CA mutations. Mod Pathol. 25:615–624. [PubMed: 22157930]
34. Zhao L, Vogt PK. Helical domain and kinase domain mutations in p110alpha of phosphatidylinositol 3-kinase induce gain of function by different mechanisms. Proc Natl Acad Sci U S A. 2008; 105:2652–2657. [PubMed: 18268322]
35. Adams JR, et al. Cooperation between Pik3ca and p53 mutations in mouse mammary tumor formation. Cancer research. 2011; 71:2706–2717. [PubMed: 21324922]

36. Kinross KM, et al. An activating Pik3ca mutation coupled with Pten loss is sufficient to initiate ovarian tumorigenesis in mice. The Journal of clinical investigation. 2012; 122:553–557. [PubMed: 22214849]
37. Lowery WJ, et al. Loss of ARID1A-associated protein expression is a frequent event in clear cell and endometrioid ovarian cancers. Int J Gynecol Cancer. 2012; 22:9–14. [PubMed: 22193641]
38. Offman SL, Longacre TA. Clear cell carcinoma of the female genital tract (not everything is as clear as it seems). Adv Anat Pathol. 2012; 19:296–312. [PubMed: 22885379]
39. Hendrix ND, Wu R, Kuick R, Schwartz DR, Fearon ER, Cho KR. Fibroblast growth factor 9 has oncogenic activity and is a downstream target of Wnt signaling in ovarian endometrioid adenocarcinomas. Cancer research. 2006; 66:1354–1362. [PubMed: 16452189]
40. Yamaguchi K, et al. Identification of an ovarian clear cell carcinoma gene signature that reflects inherent disease biology and the carcinogenic processes. Oncogene. 2010; 29:1741–1752. [PubMed: 20062075]
41. Yanaihara N, et al. Cytokine gene expression signature in ovarian clear cell carcinoma. Int J Oncol. 2012; 41:1094–1100. [PubMed: 22751940]
42. Anglesio MS, et al. IL6-STAT3-HIF signaling and therapeutic response to the angiogenesis inhibitor sunitinib in ovarian clear cell cancer. Clinical cancer research : an official journal of the American Association for Cancer Research. 2011; 17:2538–2548. [PubMed: 21343371]
43. Naugler WE, Karin M. The wolf in sheep's clothing: the role of interleukin-6 in immunity, inflammation and cancer. Trends Mol Med. 2008; 14:109–119. [PubMed: 18261959]
44. Guo Y, Xu F, Lu T, Duan Z, Zhang Z. Interleukin-6 signaling pathway in targeted therapy for cancer. Cancer Treat Rev. 2012; 38:904–910. [PubMed: 22651903]
45. Vasudevan KM, et al. AKT-independent signaling downstream of oncogenic PIK3CA mutations in human cancer. Cancer Cell. 2009; 16:21–32. [PubMed: 19573809]
46. Jia S, et al. Essential roles of PI(3)K-p110beta in cell growth, metabolism and tumorigenesis. Nature. 2008; 454:776–779. [PubMed: 18594509]
47. Ness RB, Cottreau C. Possible role of ovarian epithelial inflammation in ovarian cancer. Journal of the National Cancer Institute. 1999; 91:1459–1467. [PubMed: 10469746]
48. Wiegand KC, et al. ARID1A mutations in endometriosis-associated ovarian carcinomas. N Engl J Med. 363:1532–1543. [PubMed: 20942669]
49. Samartzis EP, et al. Loss of ARID1A/BAF250a-expression in endometriosis: a biomarker for risk of carcinogenic transformation? Mod Pathol. 25:885–892. [PubMed: 22301703]
50. Wiegand KC, et al. Loss of BAF250a (ARID1A) is frequent in high-grade endometrial carcinomas. J Pathol. 224:328–333.
51. Somigliana E, et al. Use of the concomitant serum dosage of CA 125, CA 19-9 and interleukin-6 to detect the presence of endometriosis. Results from a series of reproductive age women undergoing laparoscopic surgery for benign gynaecological conditions. Hum Reprod. 2004; 19:1871–1876. [PubMed: 15218003]
52. Darai E, Detchev R, Hugol D, Quang NT. Serum and cyst fluid levels of interleukin (IL) -6, IL-8 and tumour necrosis factor-alpha in women with endometriomas and benign and malignant cystic ovarian tumours. Hum Reprod. 2003; 18:1681–1685. [PubMed: 12871882]
53. Chang Q, Daly L, Bromberg J. The IL-6 feed-forward loop: a driver of tumorigenesis. Seminars in immunology. 2014; 26:48–53. [PubMed: 24613573]
54. Liu P, Jenkins NA, Copeland NG. A highly efficient recombineering-based method for generating conditional knockout mutations. Genome Res. 2003; 13:476–484. [PubMed: 12618378]
55. Brachmann SM, et al. Characterization of the mechanism of action of the pan class I PI3K inhibitor NVP-BKM120 across a broad range of concentrations. Mol Cancer Ther. 2012; 11:1747–1757. [PubMed: 22653967]
56. Roberts PJ, et al. Combined PI3K/mTOR and MEK inhibition provides broad antitumor activity in faithful murine cancer models. Clinical cancer research : an official journal of the American Association for Cancer Research. 2012; 18:5290–5303. [PubMed: 22872574]
57. Chen Z, et al. A murine lung cancer co-clinical trial identifies genetic modifiers of therapeutic response. Nature. 2012; 483:613–617. [PubMed: 22425996]

58. The genome architecture of the Collaborative Cross mouse genetic reference population. Genetics. 2012; 190:389–401. [PubMed: 22345608]

59. Van Loo P, et al. Allele-specific copy number analysis of tumors. Proceedings of the National Academy of Sciences of the United States of America. 2010; 107:16910–16915. [PubMed: 20837533]

60. Cerami E, et al. The cBio cancer genomics portal: an open platform for exploring multidimensional cancer genomics data. Cancer Discov. 2012; 2:401–404. [PubMed: 22588877]

61. Gao J, et al. Integrative analysis of complex cancer genomics and clinical profiles using the cBioPortal. Sci Signal. 2013; 6:l1.

62. Bolstad BM, Irizarry RA, Astrand M, Speed TP. A comparison of normalization methods for high density oligonucleotide array data based on variance and bias. Bioinformatics. 2003; 19:185–193. [PubMed: 12538238]

63. Smyth GK. Linear models and empirical bayes methods for assessing differential expression in microarray experiments. Stat Appl Genet Mol Biol. 2004; 3 Article3.

64. Tusher VG, Tibshirani R, Chu G. Significance analysis of microarrays applied to the ionizing radiation response. Proceedings of the National Academy of Sciences of the United States of America. 2001; 98:5116–5121. [PubMed: 11309499]

65. Subramanian A, et al. Gene set enrichment analysis: a knowledge-based approach for interpreting genome-wide expression profiles. Proceedings of the National Academy of Sciences of the United States of America. 2005; 102:15545–15550. [PubMed: 16199517]

66. Mootha VK, et al. PGC-1alpha-responsive genes involved in oxidative phosphorylation are coordinately downregulated in human diabetes. Nature genetics. 2003; 34:267–273. [PubMed: 12808457]

67. Shepherd TG, Theriault BL, Campbell EJ, Nachtigal MW. Primary culture of ovarian surface epithelial cells and ascites-derived ovarian cancer cells from patients. Nature protocols. 2006; 1:2643–2649. [PubMed: 17406520]

68. Flesken-Nikitin A, Hwang CI, Cheng CY, Michurina TV, Enikolopov G, Nikitin AY. Ovarian surface epithelium at the junction area contains a cancer-prone stem cell niche. Nature. 2013; 495:241–245. [PubMed: 23467088]

69. Inouye S, et al. Impaired IgG production in mice deficient for heat shock transcription factor 1. The Journal of biological chemistry. 2004; 279:38701–38709. [PubMed: 15226319]

70. Inouye S, et al. Heat shock transcription factor 1 opens chromatin structure of interleukin-6 promoter to facilitate binding of an activator or a repressor. The Journal of biological chemistry. 2007; 282:33210–33217. [PubMed: 17766920]

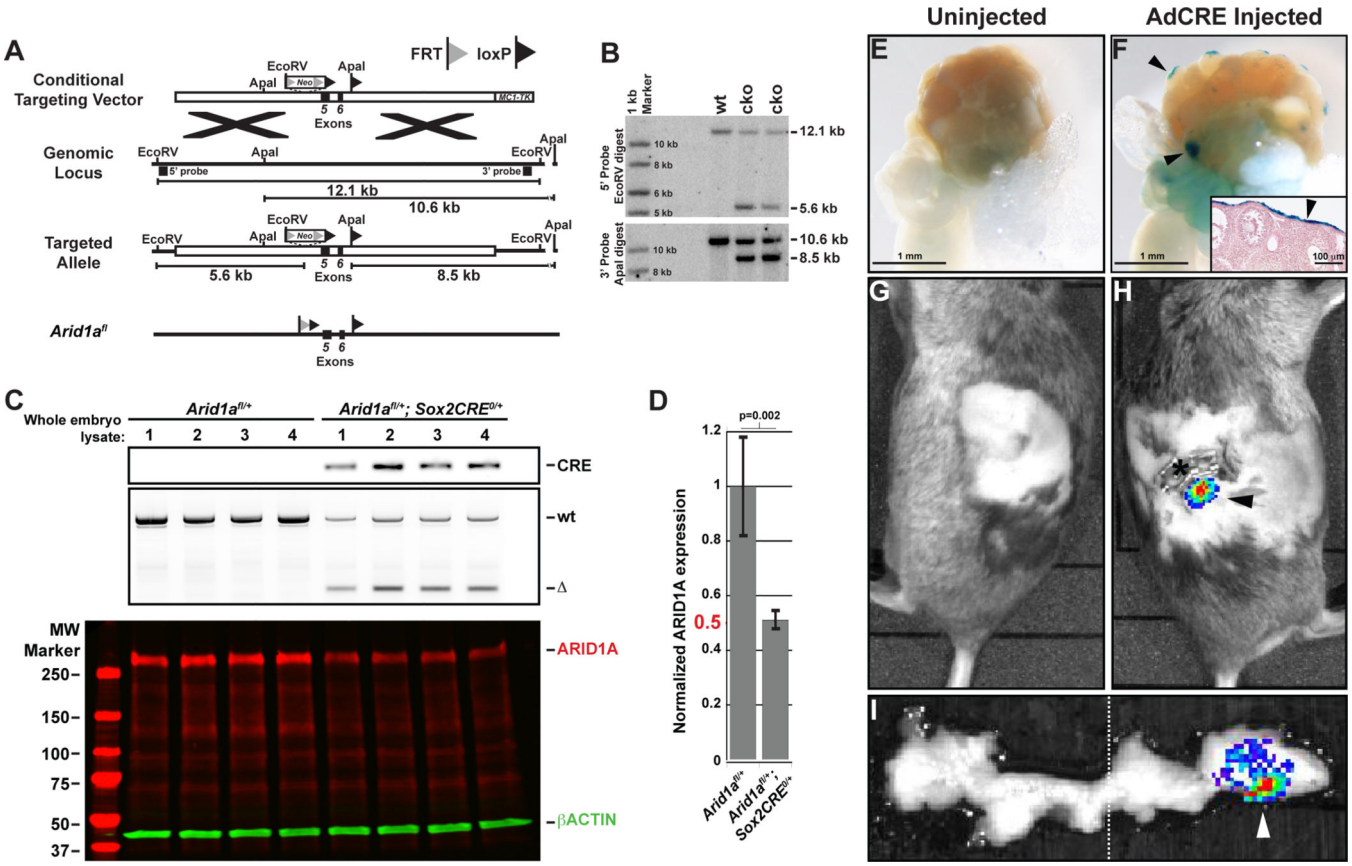

Figure 1. A new *Arid1a* conditional allele to explore ARID1A tumor suppressor function *in vivo*

(A) Targeting scheme to insert two loxP sites flanking exon 5 and 6 of mouse ARID1A. (B) Representative Southern blot showing properly targeted ES cell clones. Insertion of loxP sites generates 5.6 kb EcoRV and 8.5 kb ApaI genomic fragments. (C) PCR genotyping and quantitative, dual-color fluorescent western blot of ARID1A (red) and βACTIN (green) protein expression in whole-embryo lysates from four $Arid1a^{fl/+}$ and four $Arid1a^{fl/+}$;$Sox2Cre^{0/+}$ embryos. (D) Graph of quantitative western blot results depicting normalized protein levels. Significant differences based on the average normalized protein expression ±SD of four independent embryos were calculated using a two-tailed Student's *t* test (p-values <0.05 were considered significant). (E,F) Representative LacZ-stained, control (uninjected) or intrabursal AdCRE-injected *(Gt)Rosa26lacZ* ovary showing patterns of CRE-mediated recombination in the ovarian surface epithelium. (F, inset) Histological section of LacZ-stained AdCRE-injected *(Gt)Rosa26lacZ* ovary. (G-I) Live-luminescence overlaid whole-mount images of an intrabursal AdCRE injected, *(Gt)Rosa26luciferase* female mouse. (I) Excised reproductive tract. Asterisks in *H* indicate wound staple.

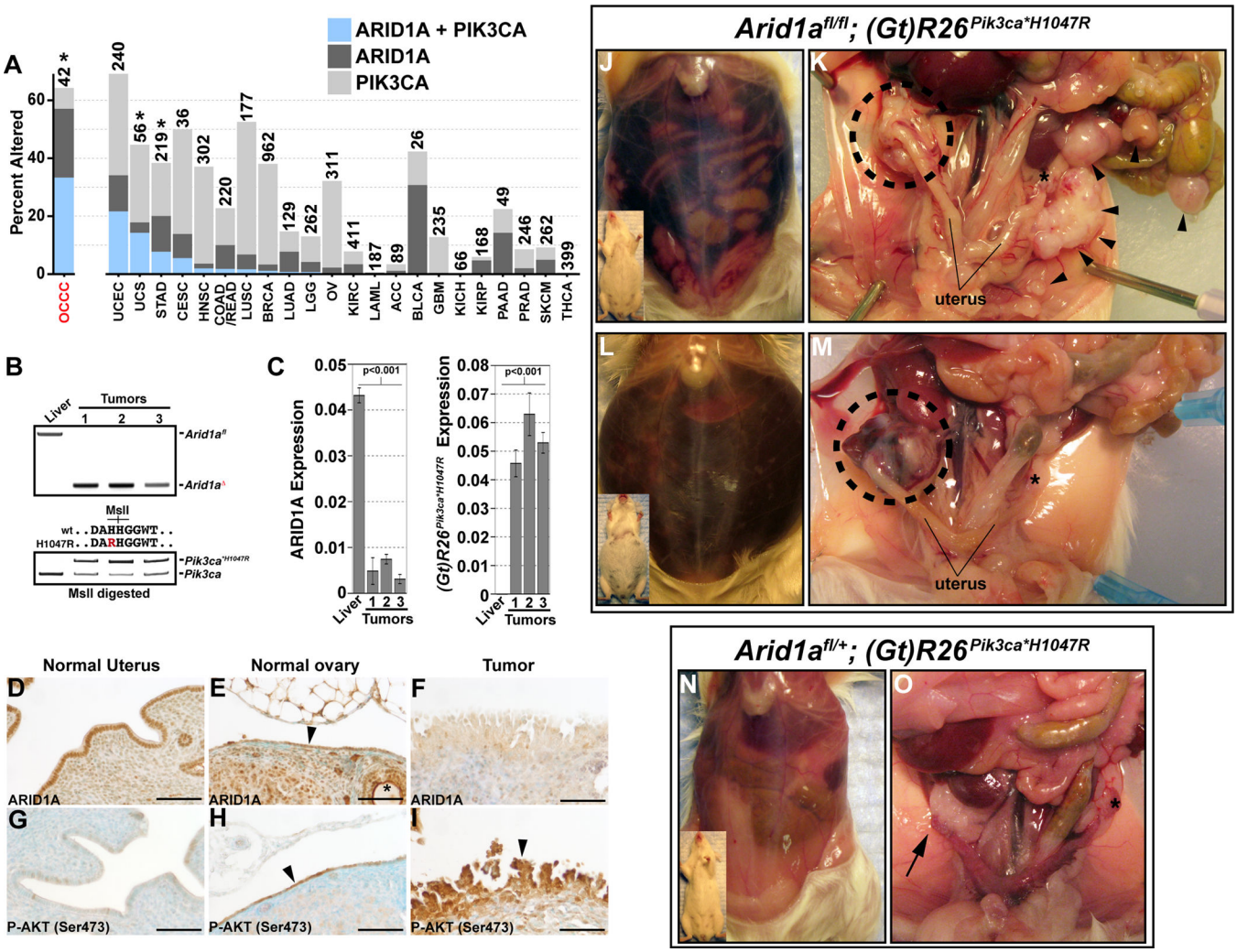

Figure 2. Concurrent ARID1A loss and PIK3CA activation leads to ovarian tumorigenesis in the mouse

(A) Plot of ARID1A and PIK3CA alterations across available TCGA datasets. Mutation or co-mutation frequencies are expressed as a percentage of all tumor samples for each cancer. A Fisher's exact test was used to calculate the significance of association between ARID1A and PIK3CA mutations (*p-value <0.05). (B) Genotyping scheme to detect CRE-deleted (*Arid1a*Δ) allele in tumor genomic DNA samples. RT-PCR was used to distinguish *PIK3CA* and transgenic *(Gt)Rosa26Pik3ca*^{*H1047R} transcripts in tumor RNA samples. The H1047R mutation in *(Gt)Rosa26Pik3ca*^{*H1047R} protects against MslI digest of amplified tumor cDNA. (C) ARID1A loss or *(Gt)Rosa26Pik3ca*^{*H1047R} transcripts were detected in tumor RNA samples by RT-PCR. Significant differences based on the average normalized mRNA expression ±SD between replicates of a control liver sample and replicates of three independent tumor samples were calculated using a two-tailed Student's *t* test (p-values <0.05 were considered significant). (D,E) ARID1A expression is observed in cells throughout the normal uterus and ovary by IHC. (E) ARID1A is expressed in the OSE of normal ovaries (arrowhead). (F) ARID1A expression is not observed in the tumors. (E) P-AKT S473 levels are low in the normal uterus. (H, I) P-AKT S473 in the normal ovary is

highest in the OSE (E, arrowhead) and these levels are greatly increased in ovarian tumors (F, arrowhead). Asterisk in *E* denotes an oocyte. All sections processed for IHC were lightly counter-stained with methyl green. (J,K) Morbid *Arid1a*$^{fl/fl}$*;(Gt)Rosa26Pik3ca*^{*H1047R} mouse at sacrifice with hemorrhagic ascites (inset), primary ovarian tumor of moderate size, and bilateral tumor metastases (arrowheads). (L,M) Morbid *Arid1a*$^{fl/fl}$*; (Gt)Rosa26Pik3ca*^{*H1047R} mouse at sacrifice with hemorrhagic ascites (inset), large primary ovarian tumor, and no visible metastases. The mice shown in *J-M* were sacrificed at 7 and 9 weeks post-AdCRE, respectively, because of visible ascitic fluid burden. (N,O) *Arid1a*$^{fl/+}$*; (Gt)Rosa26Pik3ca*^{*H1047R} mice at 11-weeks post-AdCRE showing no evidence for tumor formation. In *K* and *M*, dashed circles indicate primary ovarian tumor on injected ovary. In *N*, arrows denote the AdCRE injected ovary. In *K*, *M*, and *O*, asterisks denote the uninjected, control ovary. UCEC, uterine corpus endometrial carcinoma; UCS, uterine carcinosarcoma; STAD, stomach adenocarcinoma; CESC, cervical squamous cell carcinoma and endocervical adenocarcinoma; HNSC, head and neck squamous cell carcinoma; COAD/READ, colon and rectum adenocarcinoma; LUSC, lung squamous cell carcinoma; BRCA, breast invasive carcinoma; LUAD, lung adenocarcinoma; LGG, brain lower grade glioma; OV, ovarian serous cystadenocarcinoma; KIRC, kidney renal clear-cell carcinoma; LAML, acute myeloid leukemia; ACC, adrenocortical carcinoma; BLCA, bladder urothelial carcinoma; GBM, glioblastoma multiforme; KICH, kidney chromophobe; KIRP, kidney renal papillary cell carcinoma; PAAD, pancreatic adenocarcinoma; PRAD, prostate adenocarcinoma; SKCM, skin cutaneous melanoma; THCA, thyroid carcinoma.

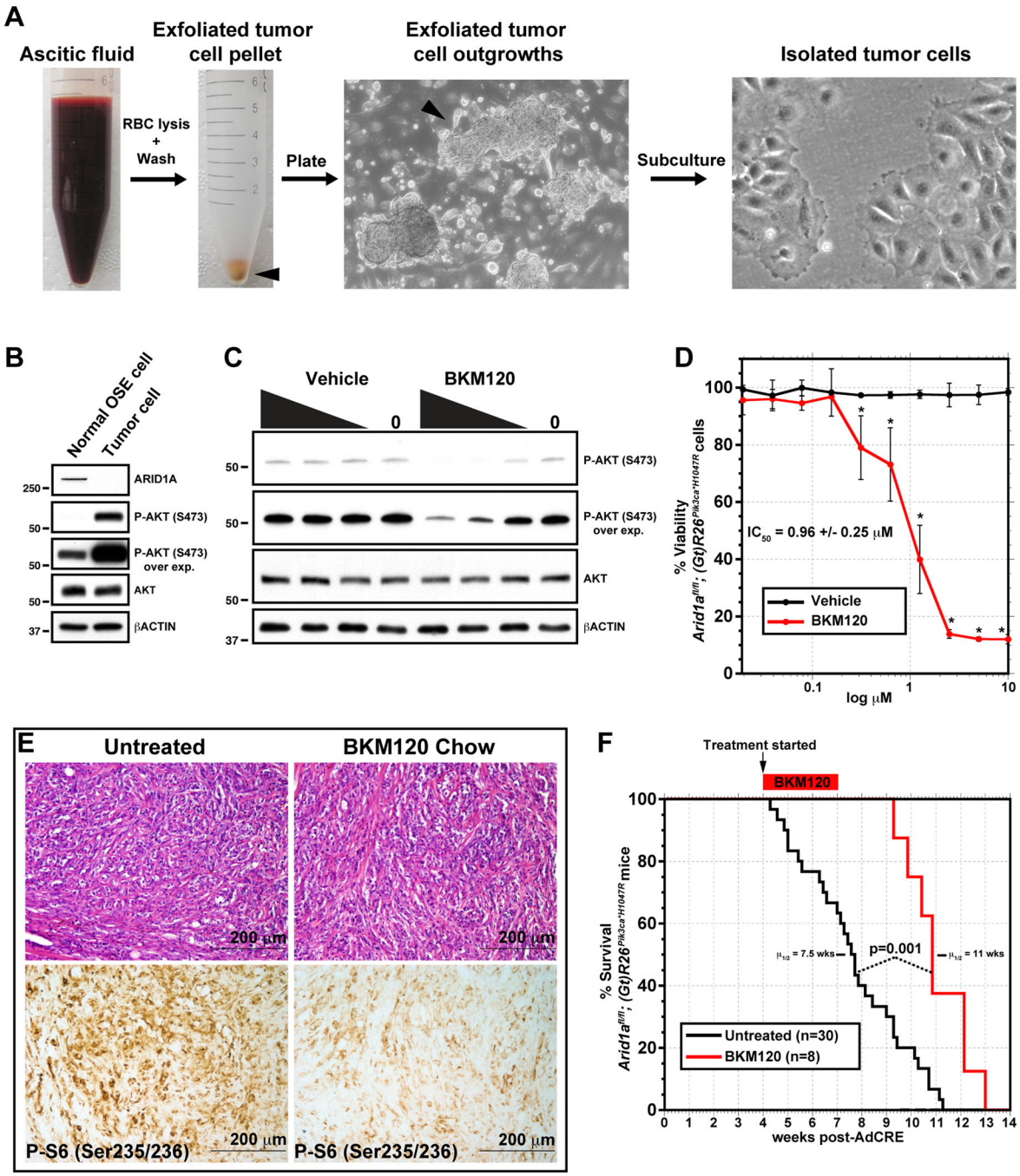

Figure 3. Therapeutic PIK3CA inhibition promotes animal survival by reducing tumor cell viability

(A) Primary ascites-derived tumor cell isolation scheme. (B) Representative western blots to highlight the primary tumor cell validation scheme and demonstrate that ARID1A loss and heightened P-AKT S473 is observed in primary *Arid1a*$^{fl/fl}$*;(Gt)Rosa26Pik3ca*^{*H1047R} ascitic tumor cells versus normal ovarian surface epithelial (OSE) cells. (C) Western blots of P-AKT S473 and total AKT levels in *Arid1a*$^{fl/fl}$*;(Gt)Rosa26Pik3ca*^{*H1047R} ascitic tumor cells grown in the presence 10, 1, 0.001, or 0 μM BKM120 or equivalent dilutions (v/v) of DMSO vehicle control for 48 hrs. (D) BKM120 treatment reduces tumor cell viability with a

half-maximal inhibitory concentration (IC_{50}) of 0.96 +/− 0.25 μM. Significant differences based on the average percent inhibition ±SD of three independent tumor cell lines treated with BKM120- versus vehicle-treated cells were calculated using a two-tailed Student's *t* test (*p-value <0.05). (E,F) Administration of chow-fed BKM120 reduces PI3K pathway activity, as shown by reduced P-S6 Ser235/236 levels, and extends the *Arid1a*$^{fl/fl}$*;(Gt)Rosa26Pik3ca*^{*H1047R} median survival latency to 11 weeks. BKM120 treatment commenced 4 weeks after AdCRE injection. P-S6 Ser235/236 IHC was performed on tumor histological sections from three independent BKM120 treated or untreated mice. (F) Untreated *Arid1a*$^{fl/fl}$*;(Gt)Rosa26Pik3ca*^{*H1047R} mice succumb to cancer with a median ($\mu_{1/2}$) latency of period of 7.5 weeks. Statistical differences in survival (BKM120 chow-fed versus untreated) were calculated using a log rank test (p-values <0.05 were considered significant).

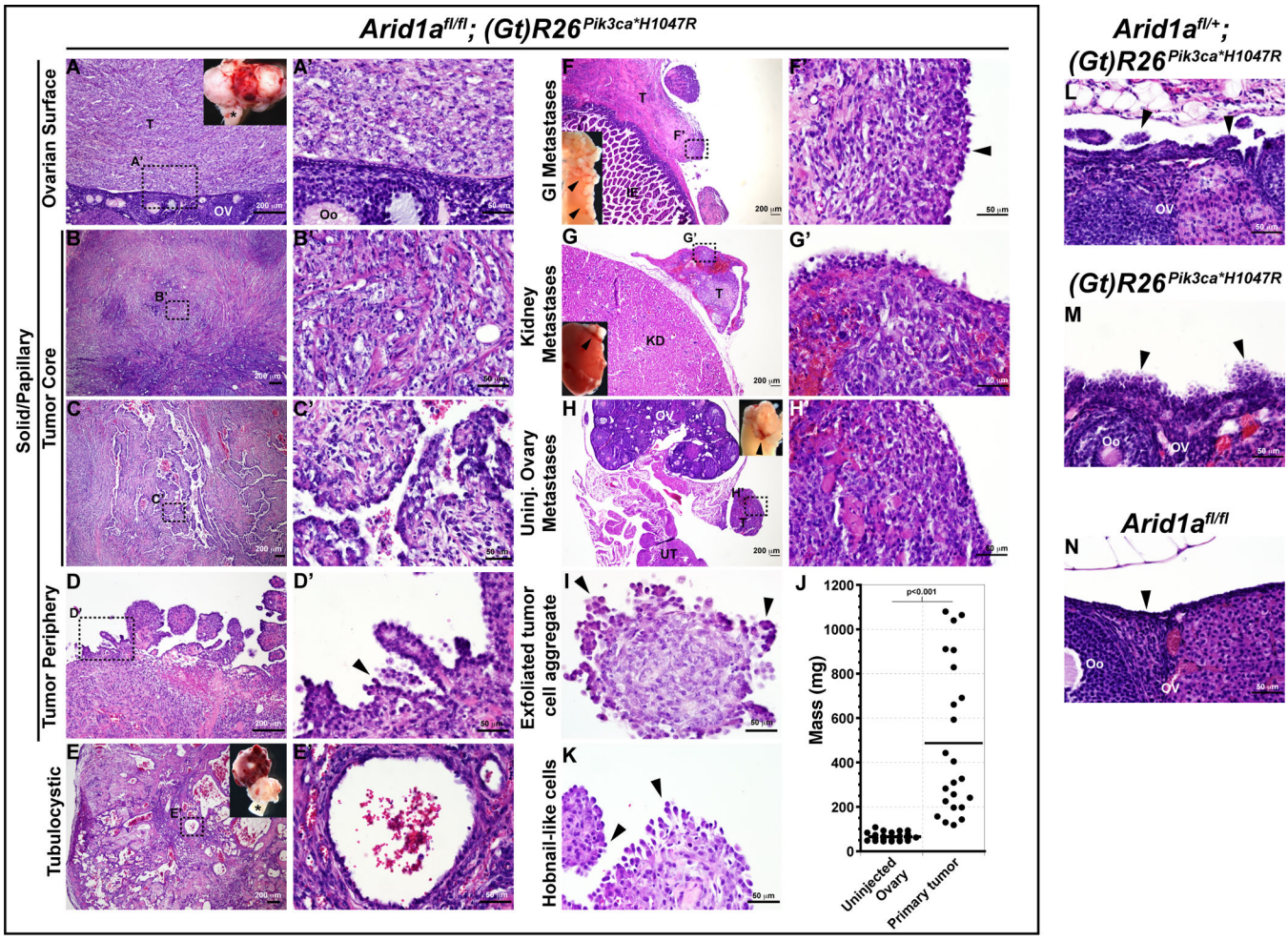

Figure 4. *Arid1a*$^{fl/fl}$*;(Gt)Rosa26Pik3ca*^{*H1047R} ovarian tumors manifest clear-cell-like histological features

(A–E) Hematoxylin and Eosin (H&E) stained sections of tumor architectural patterns observed in intrabursal AdCRE-injected *Arid1a*$^{fl/fl}$*;(Gt)Rosa26Pik3ca*^{*H1047R} mice. Whole-mount tumor images are shown inset in *A* and *E*. Asterisks denote the uterus. Dotted line *A'* demarcates the ovarian surface-tumor boundary. Arrowhead in *D'* denotes a hobnail cell. (F–H) H&E stained sections of *Arid1a*$^{fl/fl}$*;(Gt)Rosa26Pik3ca*^{*H1047R} tumor metastases found on the surface of gastrointestinal tract (F), kidney (G), and uninjected, control ovary (H). Panels *A'-H'* are high magnification images of regions demarcated by dashed boxes in *A-H*. (I) H&E stained exfoliated tumor cell aggregate. (K) H&E stained example of hobnail cells on the luminal surface a tumor. Arrowheads in *D'*, *F'*, *I*, and *K* denote hobnail cells on tumor surface. (J) Dot plot of primary tumor mass compared to uninjected control ovary. Significant differences based on the average mass ±SD between tumors and matched uninjected ovaries were calculated using a two-tailed Student's *t* test (p-values <0.05 were considered significant). (L–N) H&E stained high magnification images of the ovarian surface from *Arid1a*$^{fl/+}$*;(Gt)Rosa26Pik3ca*^{*H1047R}, *(Gt)Rosa26Pik3ca*^{*H1047R}, and *Arid1a*^{flfl} mice. (M,N) OSE hyperplasia (arrowheads) is observed in *(Gt)Rosa26Pik3ca*^{*H1047R} and

Arid1a$^{fl/+}$;*(Gt)Rosa26Pik3ca*^{*H1047R} mice. OV, ovary; Oo, oocyte; T, tumor; IE, intestinal epithelium; KD, kidney; OV, ovary; UT, uterus.

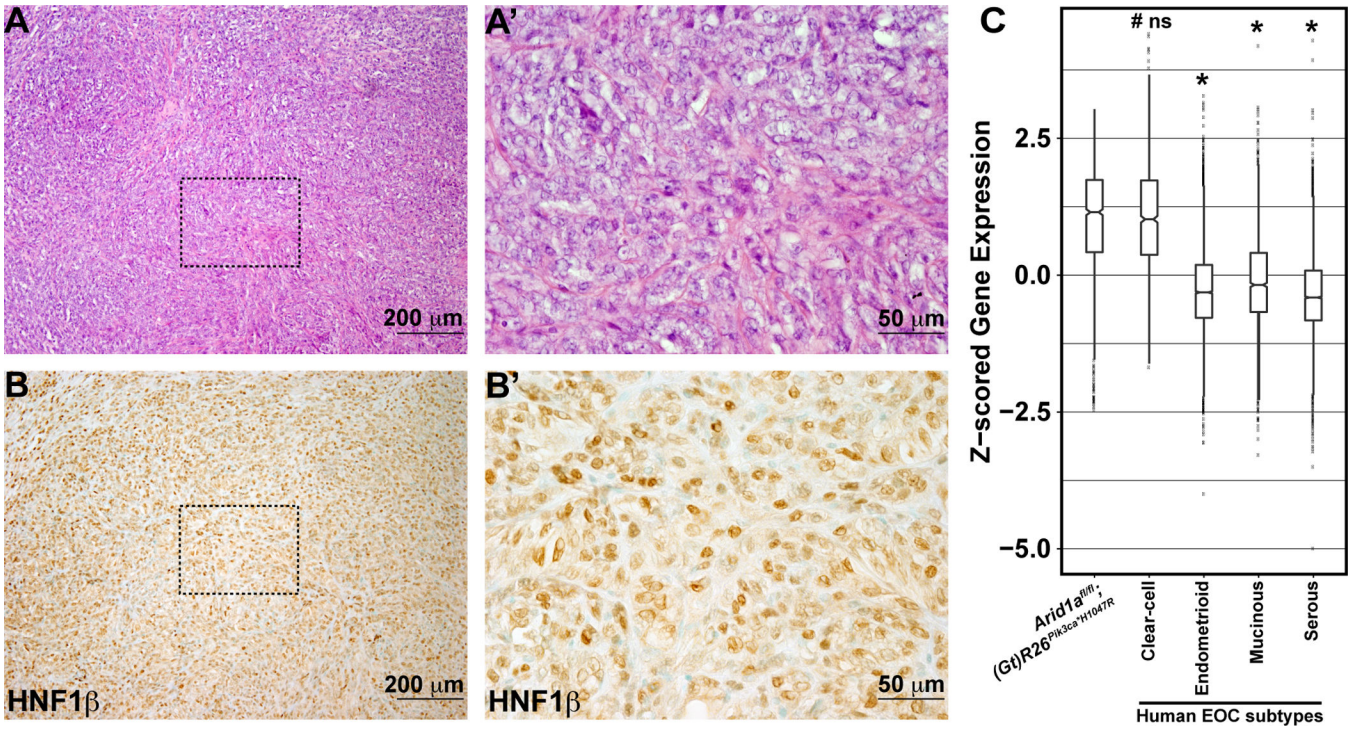

Figure 5. *Arid1a*$^{fl/fl}$*;(Gt)Rosa26Pik3ca*^{*H1047R} ovarian tumors and human OCCC share molecular characteristics

(A) H&E stained image of *Arid1a*$^{fl/fl}$*;(Gt)Rosa26Pik3ca*^{*H1047R} tumor histology. (B) Near-adjacent histological section showing HNF1β immunoreactivity by IHC. (A',B') High magnification images of regions demarcated by dashed boxes in *A* and *B*. (C) Box plots of normalized expression values of human OCCC discriminant genes (N=159) for all mouse tumor and human EOC subtype samples. Significant differences between the mouse tumors and each human histological EOC subtype were calculated using a Wilcoxon test (*significant p-value of <0.05; #not significant p-value=0.6). NS, not significant.

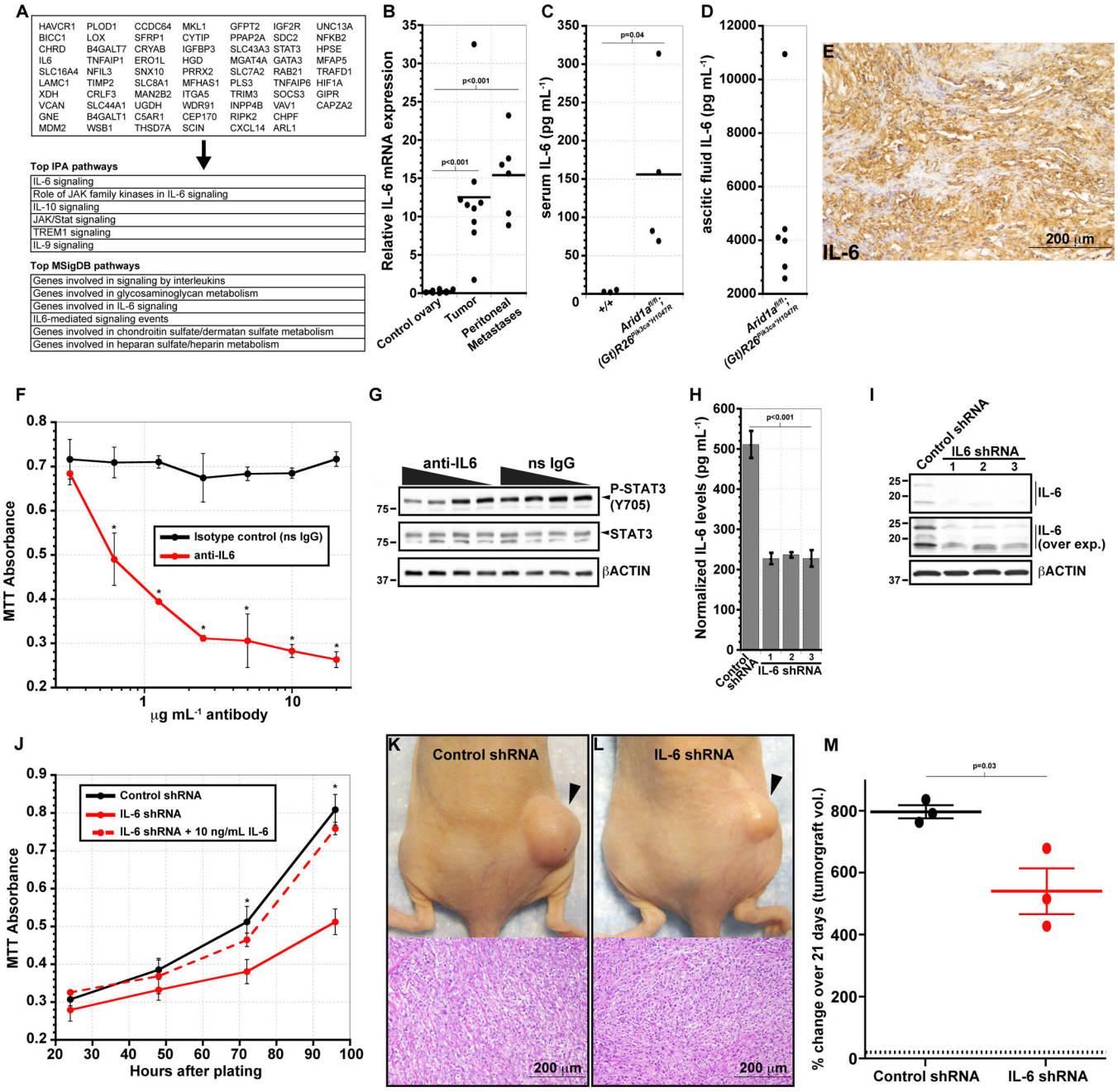

Figure 6. Tumor-derived IL-6 promotes OCCC tumor cell growth and survival

(A) Top OCCC-specific genes in common between mouse and human tumors. Top six IPA and MSigDB (GSEA) predictions of the top upregulated genes are included. (B) RT-PCR validation of IL-6 expression in primary tumors and peritoneal metastases. Significant differences based on average normalized mRNA expression ±SD between peritoneal metastases or primary tumors and matched uninjected ovaries were calculated using a two-tailed Student's *t* test. (C,D) Mouse IL-6 levels in the serum and ascitic fluid *Arid1a*$^{fl/fl}$*;* *(Gt)Rosa26Pik3ca*^{*H1047R} mice, as measured by anti-IL-6 ELISAs. Significant differences based on the average protein concentration ±SD between wild-type versus *Arid1a*$^{fl/fl}$*;*

(Gt)Rosa26Pik3ca^{*H1047R} mice were calculated using a two-tailed Student's *t* test. (E) IL-6 expression in an *Arid1a*$^{fl/fl}$*;(Gt)Rosa26Pik3ca*^{*H1047R} tumor by IHC. (F) MTT absorbance values plotted with log antibody concentration (μg mL^{-1}) for non-specific rat IgG-treated (control) or rat anti-mouse IL-6 treated *Arid1a*$^{fl/fl}$*;(Gt)Rosa26Pik3ca*^{*H1047R} ascitic tumor cells after 96 hrs. of treatment. Plot represents the average absorbance value ±SD for treatment performed on three independent cell lines. Significant differences between control- and anti-IL-6-treated cells were calculated using a two-tailed Student's *t* test (*significant p-value <0.05). (G) Primary ascitic tumor cells were treated 10, 1, 0.01, or 0 μg mL^{-1} rat anti-mouse IL-6 or non-specific Rat IgG-treated (control). (H,I) IL-6 expression in *Arid1a*$^{fl/fl}$*;(Gt)Rosa26Pik3ca*^{*H1047R} ascitic tumor cells stably expressing control shRNAs or IL-6 shRNAs by ELISA and western blot. Each replicate represents in stable pool of IL-6 shRNA expressing cells from three independently isolated tumor cell lines. Significant differences based on the average protein concentration ±SD between control- versus IL-6 shRNA were calculated using a two-tailed Student's *t* test. (J) MTT absorbance values plotted over time for control shRNA-, IL-6 shRNA-, or IL-6 shRNA-expressing cells supplemented with 10 ng/mL IL-6. Cells were plated at 2×10e4 cells per mL at hour 0, then MTT measurements were taken every 24 hours for a total of 96 hours. Significant differences between control- and IL-6-shRNA expressing cells were calculated using a two-tailed Student's *t* test (*significant p-value < 0.05). (K,L) Whole-mount images of control- and IL-6-shRNA tumorgrafts (arrowheads) on the right flank of nude mice and images of corresponding H&E-stained tumorgraft sections. (M) Plot of growth rates for control- and IL-6-shRNA expressing tumorgrafts over 21 days of measurement. Significant differences between control- and IL-6-shRNA tumorgraft growth rates were calculated using a two-tailed Student's *t* test. Only p-values <0.05 were considered significant.

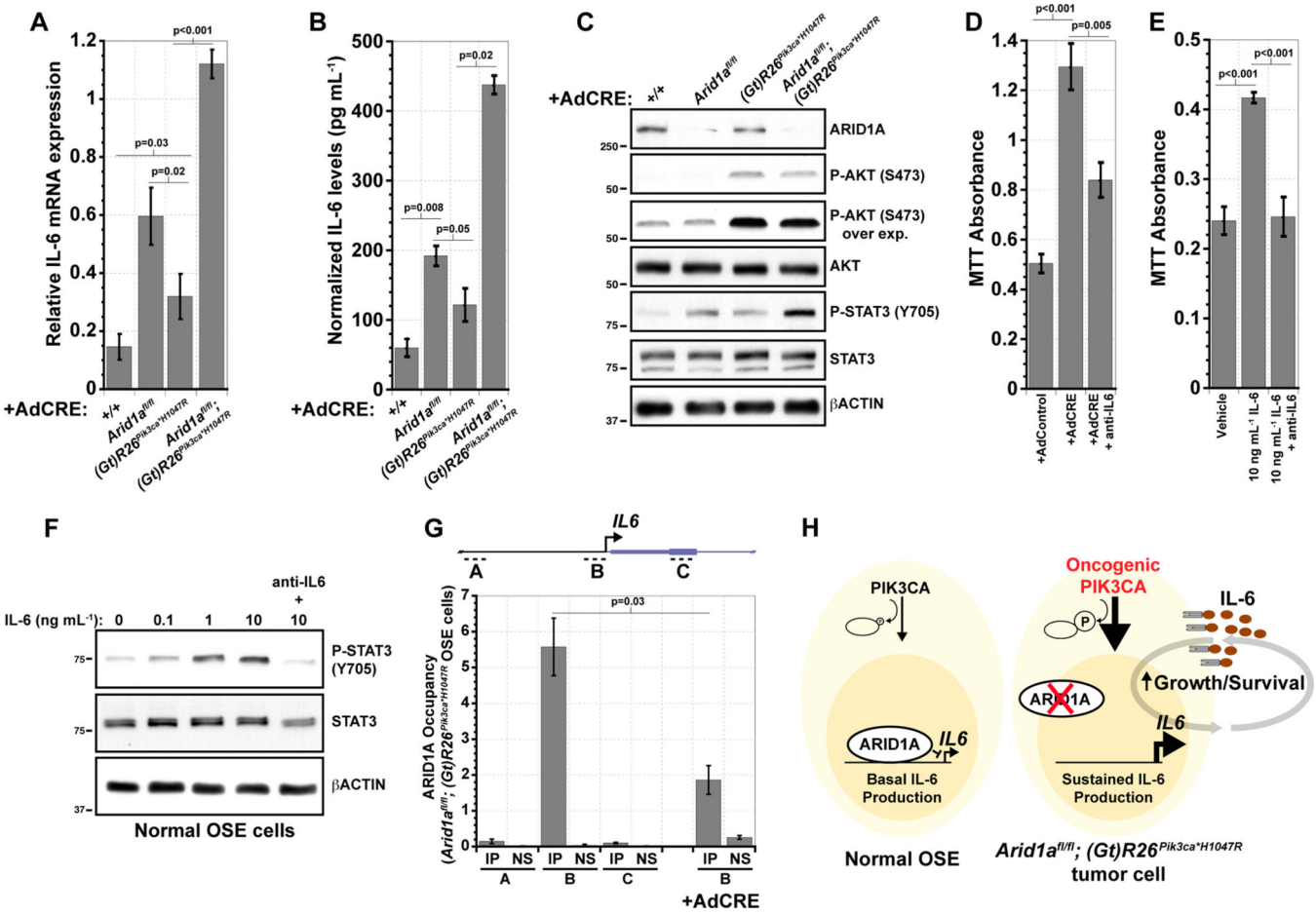

Figure 7. Coexistent ARID1A-PIK3CA mutations induce IL-6 expression in a cooperative manner

(A) IL-6 mRNA expression in AdCRE-infected primary OSE cells carrying all allele combinations. (B) Normalized IL-6 ELISA measurements of AdCRE-infected primary OSE cells carrying all allele combinations. Significant differences based on the average normalized expression value ±SD among mutant allele combinations versus wildtype were calculated using a two-tailed Student's *t* test. (C) Western blot showing ARID1A, P-AKT S473, total AKT, P-STAT3 Y705, and total STAT3 levels in AdCRE-infected primary OSE cells carrying all allele combinations. AdCRE-infected wildtype cells served as controls. (D) MTT cell viability assay on primary *Arid1a*$^{fl/fl}$*;(Gt)Rosa26Pik3ca*^{*H1047R} OSE cells treated with AdControl, AdCRE, or AdCRE supplemented with 5 μg mL^{-1} anti-IL-6 antibodies. (E) Treatment of normal (wild type) primary OSE cells with vehicle (v/v), 10 ng mL^{-1} IL-6, or 10 ng mL^{-1} IL-6 supplemented with 5 μg mL^{-1} anti-IL-6 antibodies. Significant differences based on the average MTT absorbance value ±SD between three independent replicates of AdControl- versus AdCRE-infected or vehicle versus IL-6-treated cells were calculated using a two-tailed Student's *t* test. (F) Western blot of normal primary OSE cells showing dose-dependent increases in P-STAT3 Y705 levels following IL-6 treatment. Co-treatment with 5 μg mL^{-1} anti-IL-6 antibodies blocked P-STAT3 Y705 induction. (G) ARID1A occupancy at the *IL6* locus was detected by chromatin immunoprecipitation (ChIP) using anti-ARID1A antibodies (denoted as IP) on crosslinked chromatin from AdControl- or

AdCRE-infected *Arid1a*$^{fl/fl}$*;(Gt)Rosa26Pik3ca*^{*H1047R} primary OSE cells. Non-specific isotype matched antibodies (denoted as NS) were used in control ChIPs. ARID1A occupancy at the *IL6* promoter (site or primer pair B) is reduced in ARID1A depleted cells treated with AdCRE. Average percent ChIP input ±SD represent data from experiments performed using three primary OSE cell isolations. Significant differences were calculated using a two-tailed Student's *t* test. (H) Proposed model of IL-6 regulation by ARID1A and PIK3CA mutations in OCCC. Only p-values <0.05 were considered significant.

Nat Commun. Author manuscript; available in PMC 2015 July 27.

Table 1

Ovarian tumorigenesis requires concurrent ARID1A loss and PIK3CA activation

	[1] *Arid1a*$^{fl/fl}$; *Gt(Rosa)26*^{Pik3ca*H1047R}	[1] BKM120 treated *Arid1a*$^{fl/fl}$; *Gt(Rosa)26*^{Pik3ca*H1047R}	[2] *Arid1a*$^{fl/+}$; *Gt(Rosa)26*^{Pik3ca*H1047R}	[2] *Arid1a*$^{fl/fl}$	[2] *Gt(Rosa)26*^{Pik3ca*H1047R}
OSE hyperplasia[3]	-	-	5/7 (71%)	0/6 (0%)	4/5 (80%)
Ascites	12/30[a] (40%)	6/10[f] (60%)	0/8 (0%)	0/47[b] (0%)	0/6 (0%)
Primary ovarian tumors (Injected side)	23/30[c,d,e] (77%)	8/10[f] (80%)	0/8 (0%)	0/47[b] (0%)	0/6 (0%)
Papillary/Solid[3]	6/12 (50%)	-	-	-	-
Tubulocystic[3]	2/12 (17%)	-	-	-	-
Mixed[3]	4/12 (33%)	-	-	-	-
Peritoneal metastases	17/30[c,d,e] (57%)	5/8 (63%)	0/8 (0%)	0/47[b] (0%)	0/6 (0%)
Contralateral ovarian metastases	4/30[c,d,e] (13%)	0/8 (0%)	0/8 (0%)	0/47[b] (0%)	0/6 (0%)
Contralateral peritoneal metastases	15/30[c,d,e] (50%)	4/8 (50%)	0/8 (0%)	0/47[b] (0%)	0/6 (0%)

[1] Only morbid-euthanized mice were scored.

[2] Mice were euthanized and scored at the end of the 11-week observation period.

[3] Scored by histology.

[a] 3 mice found dead and not scored for ascites.

[b] Mice aged one-year included.

[c] 4 mice were found dead and not scored for tumor histology.

[d] 2 mice had tumors within the body wall at incision site that were likely the result of leaky AdCRE and were not scored.

[e] 1 mouse had a very large uterine tumor that was likely the result of leaky AdCRE into the lumen of the oviduct or uterus and was not scored.

[f] 2 mice found dead after treatment and not scored for ascites or primary tumors.